Title
Theory and Design of Terahertz Quantum-Cascade Littrow Metasurface External Cavity Lasers

Author
Mortazavian, Parastou

Publication Date
2020

Peer reviewed|Thesis/dissertation

UNIVERSITY OF CALIFORNIA

Los Angeles

Theory and Design of Terahertz Quantum-Cascade Littrow Metasurface External Cavity Lasers

A thesis submitted in partial satisfaction

of the requirements for the degree Master of Science

in Electrical & Computer Engineering

by

Parastou Mortazavian

2020

ABSTRACT OF THE THESIS

Theory and Design of Terahertz Quantum-Cascade Littrow Metasurface External Cavity Lasers

by

Parastou Mortazavian

Master of Science in Electrical & Computer Engineering

University of California, Los Angeles, 2020

Professor Benjamin S. Williams, Chair

Quantum-cascade vertical-external-cavity surface-emitting-laser (QC-VECSEL) is a recently developed compact and coherent source of THz radiation which has demonstrated excellent beam quality and scalable high-power. The key component of the QC-VECSEL is an amplifying reflectarray metasurface made up of an array of sub-wavelength metal-metal waveguides loaded with quantum-cascade (GaAs/AlGaAs) laser gain material. To further the usefulness of this technology for many applications, including spectroscopy, heterodyne detection, and multispectral imaging, broadband and tunable THz QCLs are required. In this work, I investigate the feasibility

of two techniques for tuning THz metasurface-based QCLs. First, A Littrow metasurface external cavity laser (ECL) is modeled and studied. We also propose and evaluate a novel method to implement Littrow ECL based upon blazed metasurface gratings. Electromagnetic simulations show that these metasurfaces can provide up to 15% fractional tunability around the center frequency of the laser at 3.3 THz. Preliminary results on several active resonant-phonon quantum-cascade materials are also obtained. Current progress on actual fabrication and device testing is reported.

The thesis of Parastou Mortazavian is approved.

Mona Jarrahi

Chee Wei Wong

Benjamin S. Williams, Committee Chair

University of California, Los Angeles

2020

To my parents Morteza Mortazavian and Keihaneh Semsar who instilled in me a passion for science and supported me along my journey with unconditional love.

Table of Contents

List of Figures

List of Tables

ACKNOWLEDGMENTS

I would like to express my deepest appreciation to my advisor, Professor Benjamin Williams, for his support and guidance throughout my graduate studies. He has been my first and best mentor during the past couple of years and provided me with invaluable advices and insights on my research as well as on my career. I also want to thank Prof. Tatsuo Itoh and Dr. Mohammad Memarian who laid the foundations of my work. Also, many thanks to our outside collaborators including John Reno at Sandia National Labratories, and Vincent Gambin at Northrop Grumman for growing our samples.

I am very thankful for my former and present labmates. This thesis would not have been possible without their help and support. I like to first thank Dr. Christopher Curwen and Dr. Luyao Xu for teaching me the fundamentals of VECSELs, for always answering my countless questions, and for their invaluable contributions. I also want to thank my other labmates, Anthony Kim, Yu Wu, Yue Shen, Eilam Morag, and Mohammad Shahili, for their friendship and help.

Finally, I am deeply grateful to my parents and my sister, Savis, for their lifelong of unconditional love and support. And my last, but not least, thank you goes to my beloved husband, Arvin Razavi, for his love, companionship, and encouragements throughout these years.

Funding: I also like to thank the National Science Foundation (NSF) for funding this project and for their generous fellowship. This material is based upon work supported by the National Science Foundation Graduate Research Fellowship Program under Grant No. DGE-1650604. Any opinions, findings, and conclusions or recommendations expressed in this material

are those of the author(s) and do not necessarily reflect the views of the National Science Foundation. Also, I want to thank UCLA Graduate Education for supporting me with Eugene V. Cota-Robles Fellowship.

Chapter 1: Introduction

1.1 Terahertz quantum-cascade lasers (QCLs)

Development of technologies that operate in the terahertz frequencies, frequencies between 300 GHz to 10 THz [1], has been traditionally impeded by the fact that THz frequencies are too high for electronic devices and too low for optical devices. Previous attempts in generating terahertz radiation using electronic devices, such as transistors and Schottky diode multipliers or photonic approaches, like down-conversion and up-multiplication faced many limitations in terms of optical power levels, operation conditions, size, and complexity [1-3]. In 2002, a novel technology for generating terahertz radiation at the milliwatt level was developed for the first time by Köhler *et al.* [4]. They demonstrated the first terahertz quantum-cascade laser (QCL) at 4.4 THz with a chirped superlattice active region, using a semi-insulating surface-plasmon (SI-SP) waveguide. Since then, terahertz QCLs have proven to be the only solid-state sources that can deliver output powers much greater than milliwatts [5]. At present, a spectral coverage from 1.2–5.6 THz [1, 6-9] has been demonstrated for terahertz QCLs. The highest operating temperature for a THz QCL is currently at 210 K in pulsed mode [10], and maximum output power that is reported is 2.4 W in pulsed mode and at 10 K [11], and 138 mW in CW mode [12]. Although these QC lasers have already proven to be very useful for many applications, scientific efforts in increasing the operating temperature and output power, improving the beam quality, and expanding the spectral coverage continues.

Due to the strong absorption of free carriers in the doped cladding layers at longer wavelengths ($\propto \lambda^2$), unique waveguide geometries have been developed for terahertz QC lasers. There are two types of waveguides that have been widely used for terahertz QC lasers: the semi-insulating surface-plasmon (SI-SP) waveguide [4], and the metal–metal (MM) waveguide [13]. MM waveguides tend to have the best high temperature performance, and SI-SP waveguides produce higher output powers and better beam patterns. The output beam from a sub-wavelength cleaved-facet MM waveguide is very divergent, and thus, outcoupling efficiency and output power in these lasers are lower. However, MM waveguide lasers benefit from lower threshold gains and higher temperature performance due to their higher confinement factors and the lower losses in the double metal layers [14]. Therefore, many techniques, including using facet-mounted lenses [15], phase-locked arrays of 2nd-order surface-emitting DFB lasers [16], third-order DFB gratings [17], and 2D photonic crystal cavities [18] have been used in the past to improve their beam patterns and output power [19]. Despite the efforts to combine high power and high-quality beam pattern in terahertz QC MM waveguides, many of the results have been far from ideal. The quantum-cascade vertical-external-cavity surface-emitting laser (QC-VECSEL) is a new approach, demonstrated by Prof. Benjamin Williams' lab in 2015, that proved to be very successful in generating high-quality beams and producing high output power.

1.2 Tunable terahertz QCLS

A key characteristic that expands THz QCLs functionality in many applications, including sensing, spectroscopy, security controls, as well as bio-medical and process diagnostics, is continuously tunable single-frequency emission. QC lasers are particularly appealing for broadband tuning as the gain material can be engineered to exhibit up to octave spanning bandwidths. To tune an

individual lasing mode, the resonator eigenfrequencies must be varied. Over the years, various technological solutions and optical configurations have been employed to tune the emission frequency of terahertz quantum-cascade lasers. Here, we have listed only a few of these approaches.

The simplest and most straightforward technique for tuning the emission frequency is changing the material refractive index through changing the temperature or the driving current. However, less than 1% tuning is generally achievable using these techniques. In DFB-QCLs, a periodic grating is patterned along the laser cavity to selectively backscatter the mode which is closest to the grating's Bragg wavelength $\lambda_B = n_{eff}\Lambda$ (for a second-order Bragg grating), where n_{eff} is the effective refractive index of the mode, and Λ is the grating period. Therefore, either n_{eff} or Λ must be varied to tune a single-mode DFB laser. Fabrication limitations hinder the latter, so typically tuning is achieved by changing the effective refractive index. Even though DFB-QCLs are great sources for generating single mode emission, it is difficult to achieve broad tuning range in these lasers (see Figure 1-1 (a)) [20].

As shown in Figure 1-1 (b), THz QCLs can also be tuned broadly by realizing heterogeneous active materials [21], similar to what is done in the mid-IR range [22]. By varying the applied bias, one of the active stages aligns properly, and therefore, the maximum of the gain curve shifts. The resulting QCL in [21] can be tuned electrically over 330 GHz. However, we should note that this approach results in discontinuous tuning and a multimode device [23].

Qin *et al.* used another approach for tuning a THz QC wire laser in 2009, depicted in Figure 1-1 (c)), that showed great potential for continuous single mode tuning (~137 GHz) [24]. By mechanically moving an object (plunger) near the wire laser, which had transverse dimensions

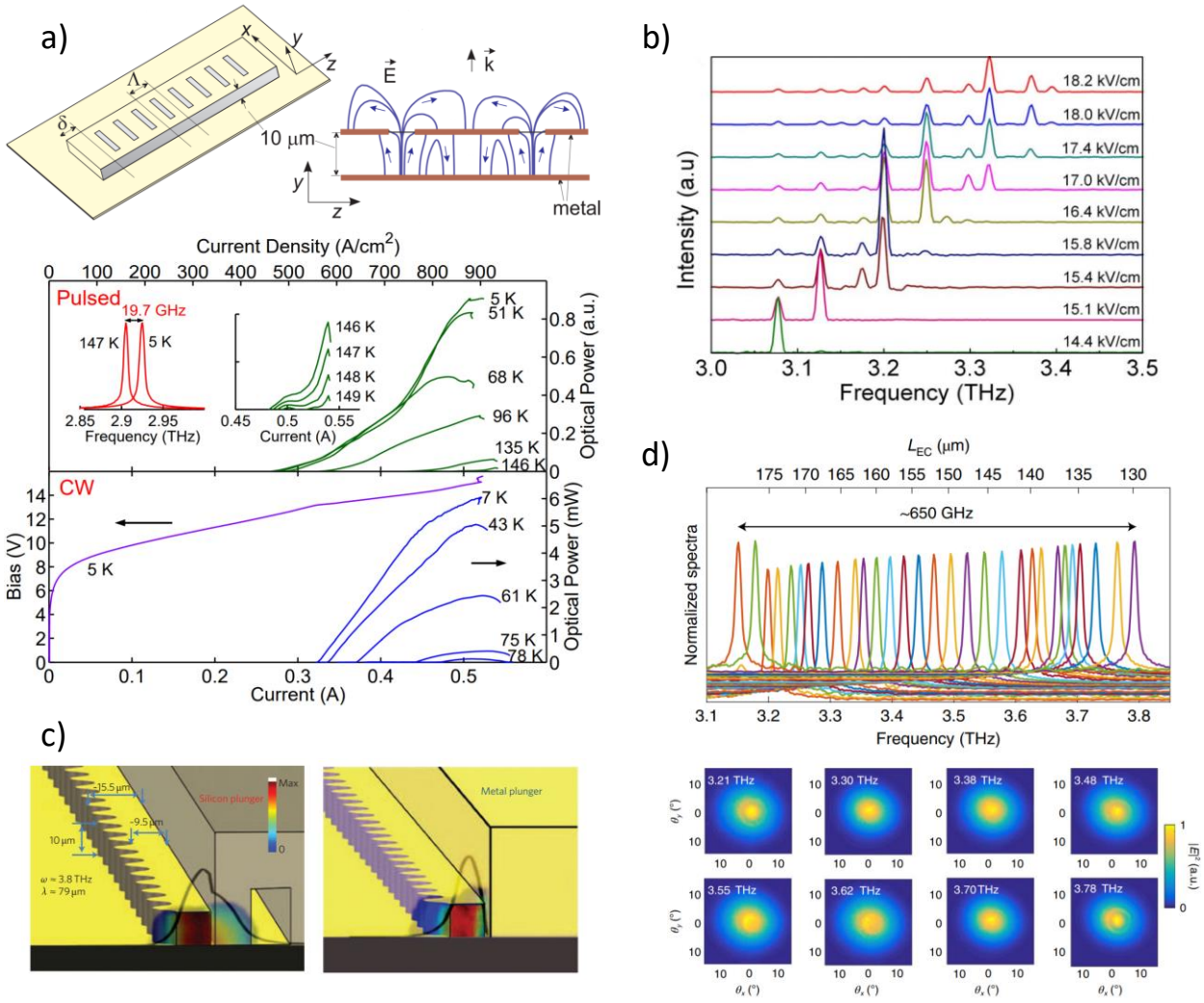

Figure 1-1: (a) The 3D schematic of the grating structure and the change in field polarization for surface emission are presented. *L-I* characteristics of the device and the single-mode temperature tuning are also shown (courtesy of Ref [20]). (b) Emission spectra of a heterogeneous design at 4K and for different applied biases are depicted (courtesy of Ref [21]). (c) Schematics of the tuning mechanism with a silicon plunger (left) and a metallic plunger (right) is illustrated (courtesy of Ref [24]). (d) Single-mode spectra of the tunable VECSEL and measured beam patterns across the tuning range are presented (courtesy of Ref [26]).

much smaller than the wavelength ($w=\lambda/3$), they could manipulate a large fraction of the mode propagating outside the cavity, and therefore tune the resonant frequency. This way, all the modes of the cavity are affected in the same way, and mode competition or mode hopping is eliminated.

Later, the same group achieved a single mode continuous tuning range of 330 GHz by fabricating a narrower ($w=\lambda/8$) laser and using a MEMS plunger [25]. However, the main drawback of this approach is that the wire laser, which in fact is a sub-wavelength MM waveguide, generates an extremely divergent beam which results in a very low outcoupling efficiency. Therefore, the output power is very low. Another problem that arises with this "mechanical tuning" approach is that the output power changes with the plunger position in a complicated way, due to the changes in the beam pattern, and therefore, it is very difficult to estimate the absolute power [23].

The final tuning scheme that we consider here is the external cavity (EC) QCL, in which frequency of the laser resonator is tuned by changing the laser cavity length. Developing external cavities using THz QCLs has been traditionally difficult because the waveguide cross-sections are considerably smaller than the free-space wavelength. It is, therefore, challenging to couple the radiation to an external element and back into the waveguide efficiently. Also, changing the cavity length could typically provide limited continuous tunability because laser cavities are usually much larger than the lasing wavelengths, which results in a small FSR (free spectral range) and therefore a small tuning range $\Delta\nu \approx$ FSR [26].

More recently, an alternative EC approach for THz QC-VECSELs has been implemented, by my graduated colleague Dr. Christopher Curwen, which provides broadband tuning while maintaining its high power and good beam quality across the tuning range (see Figure 1-1 (d)). The key component of this work is an amplifying reflect-array metasurface consisting of metal-metal ridges that are filled with QC active material (discussed further in section 1.5). Implementing short-cavity configurations for QC-VECSELs is straightforward and simple since the gain is provided by the loaded metal-metal waveguides, and therefore, reducing the cavity length does not

have detrimental effect on the laser threshold. By mechanically reducing the cavity length to sub-wavelength sizes, continuous tuning with more than 20% fractional bandwidth can be achieved [26].

1.3 Mid-infrared and terahertz Littrow external cavity lasers

A grating-coupled external cavity system is a widely used technique for tuning single-mode mid-infrared quantum-cascade lasers. Mid-infrared QC lasers with broad heterogeneous quantum-cascade active regions have demonstrated up to 39% fractional tuning around 9.5 μm using EC Littrow configurations [27]. In conventional Littrow external cavity lasers (ECL), tunable feedback is provided by a diffraction grating that retroreflects into the laser gain chip using the m=-1 diffraction order. Laser emission frequency is then tuned by changing the grating angle with respect to the incident beam, thereby shifting the frequency for maximum back-scattering.

1.3.1 Details of diffraction at a grating

Diffraction gratings were discovered in the 18th century [28], and they are widely used in spectroscopy and multi-spectral imaging applications, absorption spectroscopy of chemicals, studying the early universe, and imaging biological samples. As shown in Figure 1-2, a diffraction grating is an optical component with a periodic structure at the interface of two materials that diffracts the incident light in specific angles. The period of modulation is on the scale of the wavelength. There are two types of diffraction gratings: transmission gratings and reflection gratings, but we are only considering the latter here. The following general grating equation governs the operation of diffraction gratings [28]:

$$m\lambda = \Lambda(\sin\alpha + \sin\beta), \tag{1.3.1}$$

where Λ is the grating period, λ is wavelength, m is an integer denoting the diffraction order, and α and β denote the incidence angle and the diffraction angle respectively. m=0 diffracted beam, also called the specular reflection, is the mirror-like reflection of light from the surface and does not depend on the wavelength. However, when $m\neq0$, the angle of diffraction β depends on the wavelength, and this is why a diffraction grating is typically used as a frequency selective component in a laser resonator.

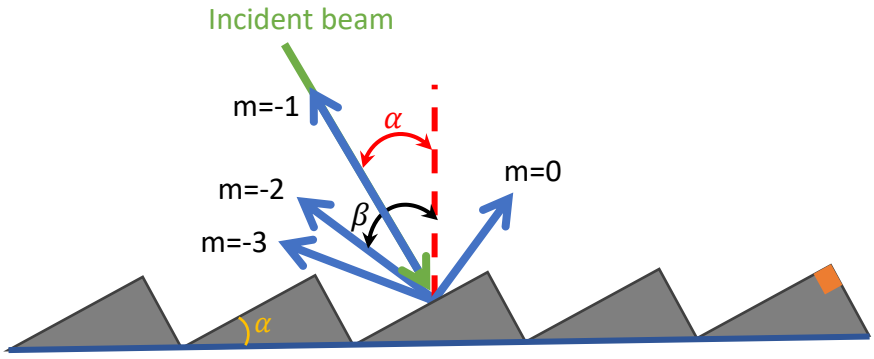

Figure 1-2: A blazed sawtooth diffraction grating

In the so-called *Littrow configuration* of a reflection grating, light is diffracted back toward the direction from which it impinges on the surface ($\alpha = \beta$). In most applications, it is the first order beam (m = -1) that satisfies the Littrow condition: $\frac{m\lambda}{\Lambda} = 2\sin\beta$. The Littrow configuration is often used in frequency tunable lasers, but to properly apply diffraction gratings as laser end mirrors, the following grating parameters must also be known: the first-order Littrow efficiency and the grating losses (or zeroth order reflection).

For any general diffraction grating structure, distribution of output power over different diffraction orders can be calculated with diffraction theory. However, it has been shown that diffraction gratings can be optimized such that most of the incoming energy is scattered into a certain diffraction order. The maximum efficiency of a grating is typically obtained with a simple smooth triangular groove profile. The slope of the corresponding surface profile must be optimized for the given conditions in terms of input angle and wavelength. In the Littrow configuration, the longer slanted edge of the grooves must be parallel to the wavefront of the incident light (see Figure 1-2).

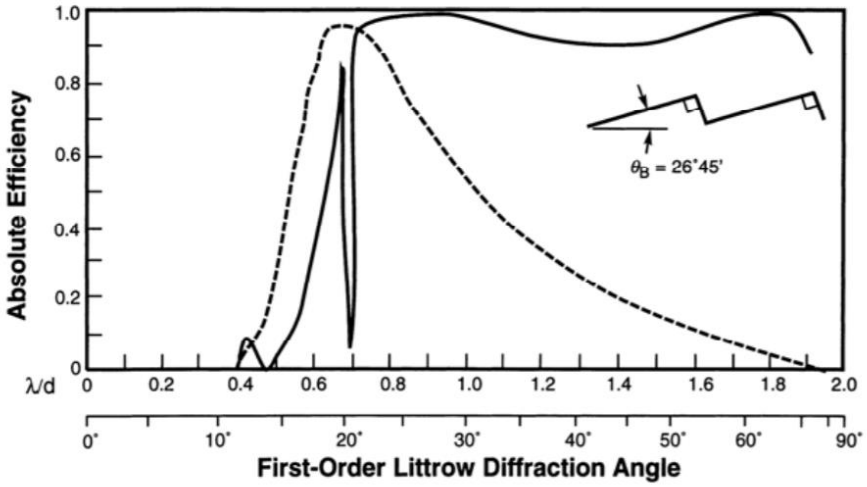

Figure 1-3: A typical theoretical first-order efficiency curve for a triangular diffraction grating with 26°45' blaze angle and Littrow mounting. Solid curve is for an incident light polarized perpendicular to the grating grooves (S-plane) and dashed curve is for light polarized parallel to the grating grooves (P-plane) (courtesy of Ref [29]).

Efficiency of a diffraction grating depends on the use conditions, wavelength and polarization of incident light, the incidence angle, diffraction order, and the groove profile and coating material (see Figure 1-3). For a reflection grating, efficiency is defined as the intensity of

monochromatic light that is diffracted, relative either to the intensity of the incident light (absolute efficiency) or to intensity of specular reflection from a polished mirror coated with the same material (relative efficiency). We should note that the total power that leaves the grating, for a given wavelength, is conserved and is equal to the power incident on it minus any scattering and absorption losses [29].

Another important characteristic of a diffraction grating is resolution power. The resolving power $R=\lambda/\Delta\lambda$ of a grating is a measure of its ability to separate adjacent spectral lines of average wavelength λ. One can show that the relative wavelength resolution $\Delta\lambda/\lambda = 1/(mN)$, where m is the diffraction order under consideration and N is the number of illuminated grooves of the grating.

1.3.2 Demonstrated Mid-IR and THz Littrow ECLs

EC-QCLs are one of the most successful tuning techniques for Mid infrared QCLs, thanks to the flexible and broadband active region designs of QCLs and the advancement in the cavity configuration optimization [30]. As mentioned previously, EC-QCLs typically utilize a diffraction grating as the frequency selective element in the cavity and are constructed in the Littrow configuration. An ideal EC-QCL with perfect optical alignment and near-zero reflection from the laser's front facet, can potentially obtain a broad tuning range over the entire gain bandwidth.

Developing tunable single-mode quantum-cascade lasers with Littrow external cavity configuration was first demonstrated by Luo et al in 2001 [31]. Using a three quantum-well active region, a tuning range of ~65 and ~88 nm was achieved at the center wavelengths of 4.5 μm and 5.1 μm, respectively. Later, with the deposition of anti-reflection (AR) coating on one chip facet, tuning range was increased to 140 nm (54 cm^{-1}). Many of the earlier works, however, were limited

by the narrow QCL gain bandwidth. In 2006, Maulini *et al.* demonstrated EC-QCLs with a tuning range of 265 cm^{-1} (24% of the center wavelength) by stacking two bound-to-continuum QC active regions in one wafer [32]. More recently, a 39% fractional tuning was achieved in a QCL with a symmetric, broad, and flat heterogenous active region design (stacking five different wavelengths) [27]. This tuning range, from ~7.5 μm to ~11.5 μm, is the broadest tuning that has been achieved in quantum-cascade lasers to this date. They could also obtain an output peak power of 1 W and average power of 15.1 mW in the pulsed mode operation. The Littrow ECL, however, is not a mode hop free approach for tuning since there is always the issue of mode hopping between the longitudinal modes of the entire cavity. But, we can realize quasi-continuous wavelength tuning in mid-infrared QCLs by using long external cavities to reduce the mode spacing [33].

Compared to monolithic tunable Mid-IR QCLs (DFB-QCL arrays [34], sampled grating QCLs [35], coupled-cavity QCLs [36] , and slot QCLs [37]), EC-QCLs provide the broadest tuning range to this date. Although they usually suffer from bulky size and expensive price, EC-QCLs are still the most successful technology available. However, to further improve performance of EC-QCLs, broader gain bandwidths, broadband anti-reflection coatings, and faster tuning schemes should be investigated. EC-QCLs are usually limited to a tuning speed of hundreds of hertz [30] due to scanning rates of the mechanical components. To increase the tuning speed of EC-QCLs, we can use components with smaller masses [38], or MOEMS-based gratings [39, 40].

Despite the success of EC approach in mid-infrared QCLs, the implementation of conventional external cavity concepts encounters several difficulties in the case of THz QCLs. First, since the waveguide cross-sections are much smaller than the free-space wavelength

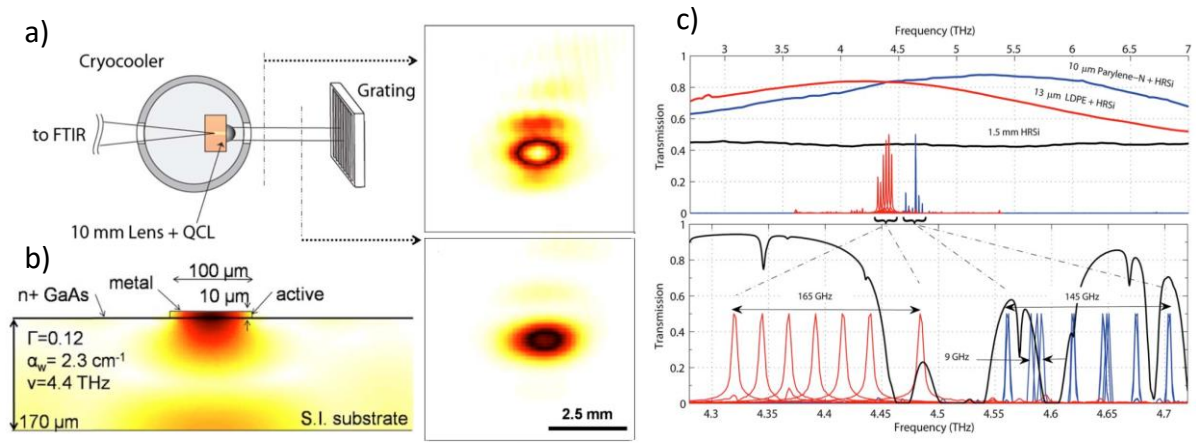

Figure 1-4: (a) An illustration of EC-QCL configuration with measured beam patterns. (b) Calculated two-dimensional fundamental mode intensity. (c)Transmission spectra of antireflection coatings that are applied to both sides of a 1.5-mm thick HR-Si window, together with unnormalized spectra of devices measuring 100 m wide by 1.5 mm long (red) and 150 m wide by 1.25 mm long (blue). The calculated atmospheric transmission through external cavity (HITRAN 2008) is also shown in black (courtesy of Ref [41]).

($w = \frac{\lambda_0}{2n}$, where n is the refractive index of QC material), it is challenging to efficiently couple the radiation to an external element and back into the waveguide. Another essential requirement for external cavity lasers is achieving near-zero facet reflectivity to effectively suppress laser oscillation in the semiconductor chip. This is typically achieved by depositing an antireflection (AR) coating on the laser's front facet. However, it is challenging to produce AR coatings that work in THz frequencies. Because of the long emission wavelengths of the order of 100 μm, the AR coating layers must be very thick. This requirement in turn creates problems in the fabrication, thickness control, and reliability. Adhesion of AR coatings to the facet under the thermal cycling conditions of laser operation is particularly problematic in THz frequencies. Also, it is difficult to find materials with appropriate refractive index and with low absorption in the this regime [23].

However, it is far more challenging to produce AR coatings for THz MM waveguide lasers compared to semi-insulating surface-plasmon (SI-SP) lasers since MM waveguides have much stronger effective facet reflectivity (typically $R \approx 30\%$ for SI-SP lasers and $R \approx 70\%$-90% for MM waveguide lasers) due to their sub-wavelength sized facets [14]. It is therefore possible to make AR coatings that work decently for SI-SP lasers. A terahertz Littrow external cavity QCL, using a QC surface-plasmon waveguide laser, was successfully demonstrated by Lee *et el.* in 2010 [41]. In this work, an EC-QCL is realized by utilizing an external grating and an antireflection-coated silicon hyperhemispherical lens, mounted on the laser's front facet (see Figure 1-4). The silicon lens reduces facet reflection and acts as a beam-forming element. This EC configuration allowed 165 GHz of single mode, discontinuous tuning and 9 GHz of continuous tuning around 4.4 THz. However, frequency hopping is observed between the longitudinal modes of the device which are spaced at 24 GHz.

1.4 Tunable QCL applications in spectroscopy and imaging

There are three main categories of applications that benefit from development of tunable THz technologies: absorption spectroscopy, heterodyne spectroscopy, and imaging. Today, high-resolution spectroscopy and imaging techniques in the THz regime require compact and robust tunable QCLs with high output power, narrow linewidth, wide and mode-hop free tunability, great beam quality, and fast response time.

Since many molecules and chemicals have rotational and vibrational transitions in the THz domain, terahertz emission or absorption spectroscopy can be used for detection of species and the study of large molecules, free radicals, ions, and reaction kinetics [42]. However, rotational

transitions of many molecules have natural and Doppler-limited linewidths that can be as narrow as a few Hz and a few hundred kHz, respectively, in this spectral range [43]. As a result, spectroscopy of low-pressure and cold gas samples needs narrow-emission sources. Tunable external cavity QCLs are particularly useful for Doppler limited absorption spectroscopy since they can provide broad tuning, narrow linewidth, and high output powers. The emission linewidth of free running THz QCLs can be as narrow as 30 kHz [44, 45], which makes them attractive for high-resolution spectroscopy. A tunable THZ DFB-QCL was, for instance, used for high-resolution spectroscopy of methanol at 2.519 THz [46]. Linewidth of THz QCLs can be furthered reduced toward the Schawlow-Townes limit (<1 kHz) by phase locking to an external element like a frequency comb [43, 47] in order to make these sources more suitable for high-resolution spectroscopy of low-pressure gas molecules. Also since the minimum detectable change of absorption in spectroscopy depends on the power per bandwidth of the source [48], QCLs are well suited for sensitive spectrometers as they generate high optical powers (up to several hundreds of mW [1]). Their high optical powers can compensate for even wider linewidths (on the order of MHz) to provide enough spectral brightness for high-resolution spectroscopy. Their broad tuning range also allows a bandwidth of several hundreds of GHz to be covered by a single laser. Tunable THz QCLs have been shown previously to perform well for Doppler limited spectroscopy of trace gases [49]. Absorption spectrum of methanol gas at high pressure and around 3.4 THz was measured using a multi-mode THz quantum-cascade laser (QCL), a grating monochromator, and a microbolometer camera [45]. In addition to absorption spectroscopy of gas molecules, tunable THz QCLs or broadband QCL-based frequency combs can be used for solid-state spectroscopy [50]. Spectroscopy of solids with broader spectral features relaxes the requirement on narrow

linewidths, but typically requires a tunability range well above 100 GHz to fully resolve the feature. On the other hand, THz radiation is non-ionizing and can propagate through many materials, including clothing, plastic, wood, and paper. These unique properties make tunable THz QCLs an attractive tool for conducting solid-state spectroscopy of concealed chemical composites, such as explosives and illicit drugs [51].

High-resolution heterodyne spectroscopy of molecular rotational lines and fine structure lines of atoms or ions, like CII line at 1.9 THz, the OH rotational transitions at 1.8 THz, 2.5 THz, and 3.5 THz, and the OI line at 4.7 THz, has always been a topic of research for the space-science community for the purpose of studying the interstellar medium and planetary atmospheres [52]. As it turns out, the universe is immersed in terahertz photons and therefore THz QCLs are receiving a lot of attention to replace the traditional local oscillators (LO) in heterodyne receivers [53, 54]. THz QCLs are compact radiation sources that can generate high optical powers in the range of 2-5 THz, but their poor beam qualities and inefficient out-coupling have hindered their development as local oscillators. In addition to great beam shape, narrow-linewidth, single mode emission, and broadband tunability are the other requirements for any excellent LO.

To date, two QCL-based heterodyne detectors have been designed and utilized in the field: (1) a 8-pixel 4.7 THz receiver designed for the Galactic/Extragalactic ULDB Spectroscopic Terahertz Observatory (GUSTO) balloon mission [55, 56], which is a follow-up mission after STO and uses a 3rd-order DFB THz QCL as a local oscillator, (2) an upgraded 7-pixel 4.7 THz heterodyne spectrometer, upGREAT (German Receiver for Astronomy at Terahertz frequencies), which utilizes a surface-plasmon QCL with a lateral 1st-order DFB grating [57, 58]. This instrument is an updated version of GREAT which was a single-pixel detector and it has flown

since 2015 on an airplane-based observatory developed and managed jointly by NASA and the German Space Agency (DLR), the Stratospheric Observatory for Infrared Astronomy (SOFIA). Both heterodyne detectors are designed for high resolution spectroscopy of neutral oxygen (OI) line at 4.745 THz.

Terahertz imaging has also received considerable attention due to several reasons. First, many materials such as paper, plastics, and ceramics, which are opaque to visible frequencies, are transparent at terahertz wavelengths. Secondly, terahertz imaging is noninvasive compared to imaging with high-energy X-rays, and provides a better spatial resolution compared to microwaves due to its shorter wavelength [59]. Lastly, the high sensitivity of THz waves to water concentrations makes this part of the electromagnetic spectrum highly suitable for bioimaging applications. Therefore, tunable THz QCL sources can be used in imaging standoff targets [60], for non-invasive security screening [61], and in multi-spectral imaging of biological samples [62, 63]. Also since terahertz QC lasers can deliver sufficient average powers to illuminate focal-plane arrays of room-temperature detectors, real-time, video-rate, terahertz imaging have been demonstrated for QC lasers [64].

1.5 Terahertz quantum-cascade VECSELs

As discussed earlier, the beam from an edge-emitting THz QC-laser with a sub-wavelength sized metal-metal waveguide is highly divergent. To improve beam quality, a novel approach was pursued by Prof. Benjamin Williams' lab in 2015. They demonstrated for the first time a quantum-cascade vertical-external-cavity surface-emitting laser (QC-VECSEL) in the terahertz regime [65]. VECSEL approach had been previously implemented successfully for inter-band semiconductor

lasers in the visible and near-infrared range [66-68] to provide high beam quality and high output powers. Its basic configuration consisted of an optically pumped semiconductor gain medium and a distributed Bragg reflector to form an optical cavity. However, according to the "intersubband selection rule" in QC-lasers, the electric field must be polarized perpendicular to the plane of the quantum well to be amplified by QC-material gain, and this is incompatible with the polarization of surface incident waves in a conventional VECSEL cavity.

Therefore, another scheme was proposed for QC-VECSELs. A QC-VECSEL consists of a large-area metasurface and an output coupler to form an external cavity laser. The metasurface is a periodic structure consisting of metallic microcavity antennas that are filled with GaAs/AlGaAs multiple-quantum-well QC-active material. Each antenna efficiently couples its TM_{01} resonance to the surface incident radiation. A high quality, near-Gaussian beam can be obtained with this approach since the radiating aperture of the THz amplifying metasurface and the external cavity optics can be made very larger (millimeter scale) than the THz wavelengths (on the order of 100 μm). A schematic of a QC-VECSEL is shown in Figure 1-5. In this section, we review the basic design and techniques used to realize the described metasurface, and the early results from THz QC-VECSEL lasers.

1.5.1 QC-VECSEL metasurface design

The building block of this thesis is the terahertz quantum-cascade vertical-external-cavity-surface-emitting-laser (QC-VECSEL) which was previously developed in our research group at UCLA. A QC-VECSEL consists of an active reflectarray metasurface reflector and an output coupler in an external-cavity configuration. The active metasurface reflector is composed of a sparse array of identical metal-metal (MM) waveguides loaded with GaAs/AlGaAs multiple-quantum-well QC

active material, as shown in Figure 1-5. The ridge width $w \approx \lambda_0/2n$ and the period Λ are designed such that the resonance occurs at the wavelength of interest λ_0. While MM waveguides are typically used to support a confined and guided mode (TEM_{00}), we want them in this case to act as surface emitting antennas. Meaning, each element couples in incident THz radiation (TM_{01}) polarized transverse to the ridge axis (x-axis, as shown in Figure 1-5 (b)), amplifies it via stimulated emission, and re-radiates it back into free space. Period Λ is therefore designed to be less than the λ_0 so that only zeroth-order (specular) reflection occurs and higher-order Bragg diffraction is suppressed.

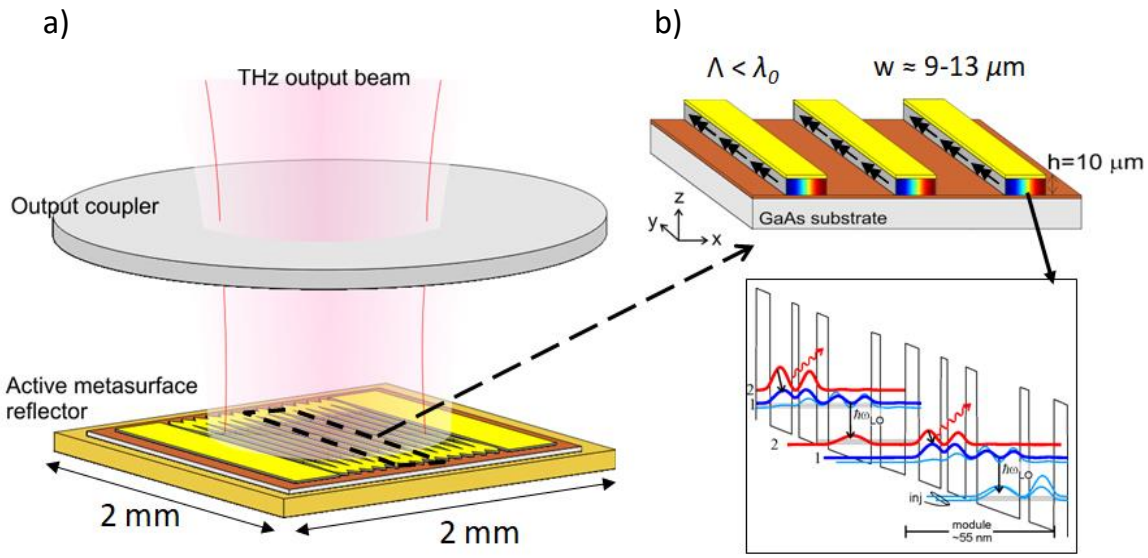

Figure 1-5: (a) Illustration of QC-VECSEL configuration including the active metasurface and output coupler. (b) Schematic of the metasurface and QC gain material. Figure is taken from Ref [65].

Numerical simulation of the metasurface reflection spectra under normal incidence of radiation (see Figure 1-6) is conducted using a full-wave finite-element electromagnetic

solver (ANSYS Electronics 19.2), in which a 3D unit cell of metasurface is modeled with Floquet periodic boundary conditions applied to represent an infinite structure. The Drude theory for conductivity was used to describe the free carrier scattering loss in QC material and gold metallization layers [69]. In this model, $\sigma(\omega)$ is derived for an electron that is placed in an electric field $\mathbf{E}(\mathrm{t}) = Re(\mathbf{E}(\omega)e^{-i\omega t})$, and the parameter *N* represents the free carrier density in the bulk material, m^* is the effective carrier mass, *e* is the carrier's charge, and τ is the free carrier effect lifetime.

$$\sigma(\omega) = \frac{Ne^2\tau}{m^*(1 - i\omega\tau)} \tag{1.2}$$

Using the frequency-dependent conductivity $\sigma(\omega)$, frequency-dependent permittivity $\epsilon(\omega)$ can be written as

$$\epsilon(\omega) = \epsilon_{core} + i\frac{\sigma(\omega)}{\omega}, \tag{1.3}$$

where ϵ_{core} is the core permittivity without the free carrier contributions. It is reasonable to approximate free carrier loss in the QC active material with the same bulk Drude model, even though the QC quantum-well material is in fact an anisotropic material system. This consideration excludes the complexity arising from the carrier confinement along the material growth direction since its description involves many uncertainties such as intersubband transition lifetime. To apply bulk Drude model to QC active material, an average carrier density and the corresponding bulk mobility are used. However, we should account for this confinement effect when the active material has a non-zero gain g. Since the intersubband gain only interacts with the electric field polarized along the growth direction (assumed to be along the *z* direction), the bulk Drude expression $\epsilon(\omega)$ should be written as an anisotropic tensor expression,

$$\epsilon(\omega) = \begin{pmatrix} \epsilon_{GaAs} & 0 & 0 \\ 0 & \epsilon_{GaAs} & 0 \\ 0 & 0 & \epsilon_{GaAs} + i\epsilon_g(\omega) \end{pmatrix}, \quad (1.4)$$

where ϵ_{GaAs} is obtained from the bulk Drude model using Equation (1.2) and (1.3), and $\epsilon_g = \frac{gc\sqrt{\epsilon_r}}{\omega}$. ϵ_r is the relative permittivity of GaAs, and c is the speed of light. The rest of the parameters that are used to estimate permittivity for QC material and gold are listed in the table below (see Table 1.1) [69].

Table 1-1: Drude parameters used for QCL active material and Au.

Material	*Core permittivity* ϵ_{core}	*Carrier density* $N(cm^{-3})$	*Effective electron mass* m^*	*Carrier lifetime* τ *at 77 K*
QCL material	12.9 ϵ_0	5×10^{15}	$0.067m_0$	0.5 ps
Au	ϵ_0	5.9×10^{22}	m_0	39 fs

A set of simulated reflectance spectra for a group of metasurfaces with different ridge widths ranging from 10-13 μm and a fixed periodicity Λ = 70 μm is presented in Figure 1-6 (c). As expected, reducing the width *w* leads to a higher resonance frequency. Figure 1-6 (a) shows that the reflectance R_{MS} increases with gain g for the metasurface with *w* = 12 μm and Λ = 70 μm which is resonant at 3.3 THz. We should also note that transparency gain g_{tr} (when R_{MS} = 1) is ~20 cm^{-1} here. In these simulations, we assume that gain g from the active medium is frequency-independent, but in fact, the gain will have its own lineshape. Therefore, we generally try to match the metasurface resonance with the peak gain frequency of the QC material by first measuring the lasing spectrum of a conventional MM waveguide QCL fabricated from the same active material, and then designing the metasurface dimensions around the measured values.

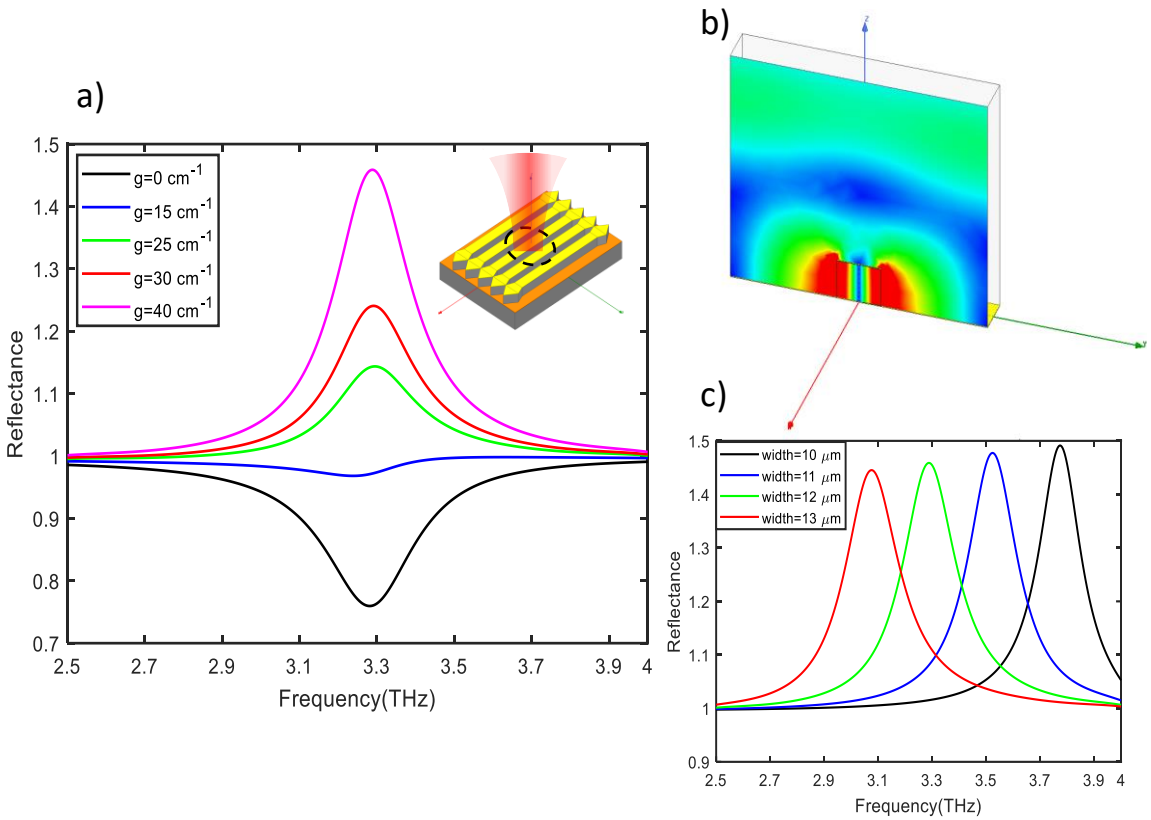

Figure 1-6: (a) Simulated reflectance of a metasurface with w = 12 μm and Λ = 70 μm for different gain g values. (b) E-field profile for the TM_{01} mode excited under normal incidence at the resonant frequency of 3.3 THz for a metasurface with w = 12 μm and Λ = 70 μm. (c) Simulated reflectance spectra for four metasurfaces with ridge widths varying from 10-13 μm and a fixed period Λ = 70 μm.

The QC-VECSEL depicted in Figure 1-5 can lase as long as the reflective gain from the amplifying metasurface is sufficient to compensate for the cavity loss and the out-coupling loss. However, an active metasurface might self-oscillate in the individual or collective sub-cavity modes since the fundamental mode requires less gain than the desired external cavity mode, and this self-lasing can be detrimental to VECSEL lasing. To tackle this problem, a few strategies are devised to engineer the loss and suppress metasurface self-lasing. First, we engineer the

metasurface to have a low radiative Q-factor for the TM_{01} mode ($Q \approx 10$, extracted from Figure 1-6 (a)) so that each sub-cavity will not self-oscillate at this mode. Second, to suppress self-lasing of each sub-cavity in the fundamental TEM_{00} guided mode, ridges are terminated with lossy boundary conditions to significantly reduce the facet reflection and thus increase the lasing threshold. To realize the lossy tapers and wire bonding area, an insulation layer is deposited between the top metal contact and the QC active material to prevent the active medium in these areas from being biased. Also, the shape of lossy tapers is designed such that waveguide mirror loss and waveguide loss are increased for TEM_{00} mode compared to TM_{01} mode. An example of this design is shown in the inset of Figure 1-6 (a).

The first uniform QC-metasurface consisted of 17 MM ridges spaced with a periodicity of $\Lambda = 90\ \mu$m and a square biased area of $1.5 \times 1.5\ mm^2$ (except tapered area) [65]. However, to reduce power consumption and to allow CW operation, the next generation of metasurfaces have been biased over a center circular area only. Except for the circular bias area in the center of metasurface, an insulation layer is deposited between the top metal contact and the QC active material to prevent the rest of the metasurface from being biased. To suppress self-lasing, the bias diameter is typically no more than half of the length of the ridges.

1.5.2 Early results

One of the early demonstrations of a THz QC-VECSEL based on a uniform metasurface is shown here [19]. This VECSEL was entirely (metasurface paired with a metal mesh output coupler) mounted inside a cryostat. The metasurface was $2 \times 2\ mm^2$, but only a center circular area of 1 mm diameter was biased. Metal-metal ridges were 11.5 μm wide and period Λ of metasurface was 70 μm. This device could generate a high peak power of 140 mW in pulsed mode at 77 K. Its slope

efficiency of 745 mW/A at 77 K was a record at the time. The peak wall-plug efficiency was 1.5%. The output coupler transmittance was about 19% in the lasing frequency range. In addition to high output power, a near-Gaussian circular beam pattern with a FWHM divergence angle of 4.9° × 4° was obtained. The measured power-current-voltage (*P-I-V)* curves, the spectra, and the 2D beam pattern for this intra-cryostat QC-VECSEL are illustrated in the figure below (see Figure 1-7).

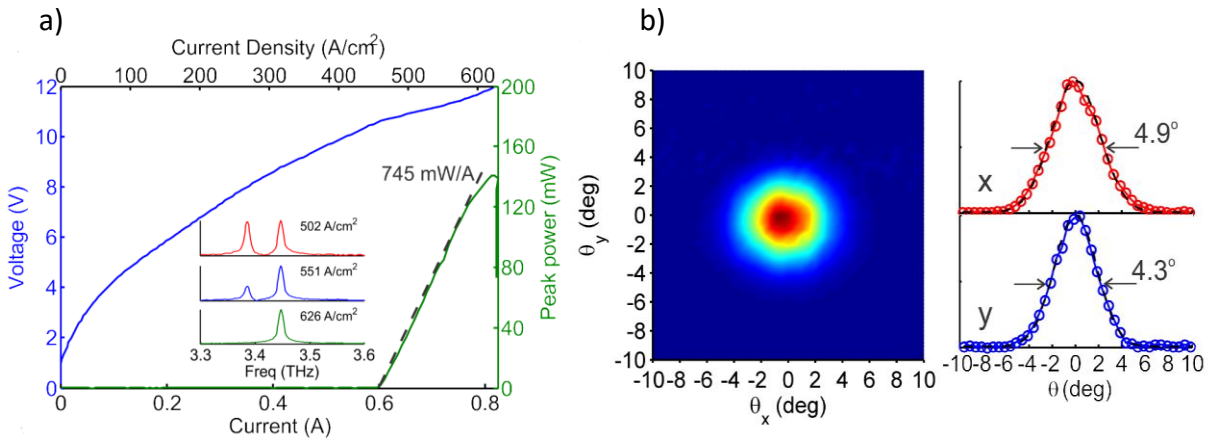

Figure 1-7: (a) Pulsed *L-I-V* data collected at 77 K for a 2×2 mm^2 metasurface (Λ = 70 μm, w = 11.5 μm) with a 1 mm bias diameter. The cavity length is ~2.5 mm and the output coupler has a transmission of ~19%. (b) Measured far-field beam pattern. Figure is taken from Ref [19].

Chapter 2: Theory and design of THz Littrow metasurface ECLs

A tunable Littrow external cavity laser (ECL) is conventionally constructed with a laser gain chip and a separate external blazed diffraction grating that retroreflects into the gain chip using the m=-1 diffraction order. As the grating is rotated, the wavelength that is consistent with retroreflection into the gain chip changes. Hence, the laser wavelength is tuned. It has recently been shown that planar metasurfaces can be constructed using patch resonant antenna elements that mimic the effect of a blazed sawtooth grating [70]. This will allow us to design the functionality of a diffraction grating into the amplifying QC-metasurface. We have investigated three possible implementations for developing a tunable Littrow metasurface ECL. In scheme 1, shown in Figure 2-1 (a), we replace a QC-waveguide laser with a QC-metasurface gain chip to build a conventional Littrow cavity using a blazed commercial diffraction grating. For schemes 2 and 3, we propose active metasurface gratings designed for "blazing" on either the 1st or 2nd diffraction orders, as depicted in Figure 2-1 (b) and Figure 2-1 (c), respectively. In these cases, the Littrow ECL will include a blazed metasurface grating and a concave mirror and the cavity is entirely constructed within a cryostat. In schemes 1 and 2, the steering zeroth order (specular) beam will be collected as the output of the laser. In scheme 3, the 1st-order beam will be the output – free from beam scanning with tuning.

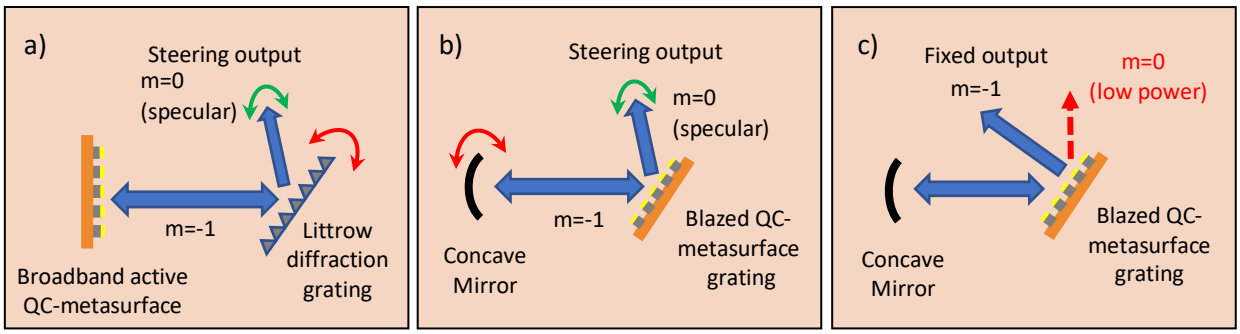

Figure 2-1: (a) A conventional Littrow metasurface external cavity laser consisting of a QC metasurface gain chip, and a separate blazed diffraction grating. (b) Schematic of a blazed 1st-order Littrow metasurface ECL is shown. (c) A blazed 2nd-order Littrow metasurface ECL is demonstrated.

2.1 Littrow ECL based upon large area Metasurfaces

To develop a broadly tunable THz QCL, we first proposed and studied a conventional Littrow ECL configuration based upon QC-metasurfaces (see Figure 2-2). This scheme is similar to previously demonstrated Littrow ECLs using SI-SP waveguide lasers [41]. However, Littrow metasurface ECL removes the necessity of having an AR-coating on the waveguide. As mentioned before, producing AR coatings that work in the THz frequencies has been one of the main challenges that hinders developing Littrow EC-QCLs. In our proposed scheme, a metasurface is mounted within an Infrared (IR) Labs dewar, and a diffraction grating is placed outside of the cryostat. An OAP mirror is also utilized to collimate the laser beam. Since a 2" × 2" Richardson diffraction grating with 7.9 grooves/mm and blaze angle of 26° 75' was purchased several years ago and was already available in our lab, we established our models and studies based upon this specific grating. This grating was designed to blaze at ~114 μm. Also, a 1"-diameter OAP mirror with a 4"-focal length was chosen to be used in the setup to extend the cavity length and to meet

the space constraints imposed by the cryostat housing. Based on the geometry of our setup and the described dimensions, we estimate the total length of the cavity (L_1+L_2) to be about 15-20 cm. We can extend the length of the cavity further as long as the laser have enough gain to overcome the losses, however, it is reasonable to limit the length to 20 cm for the first demonstrations.

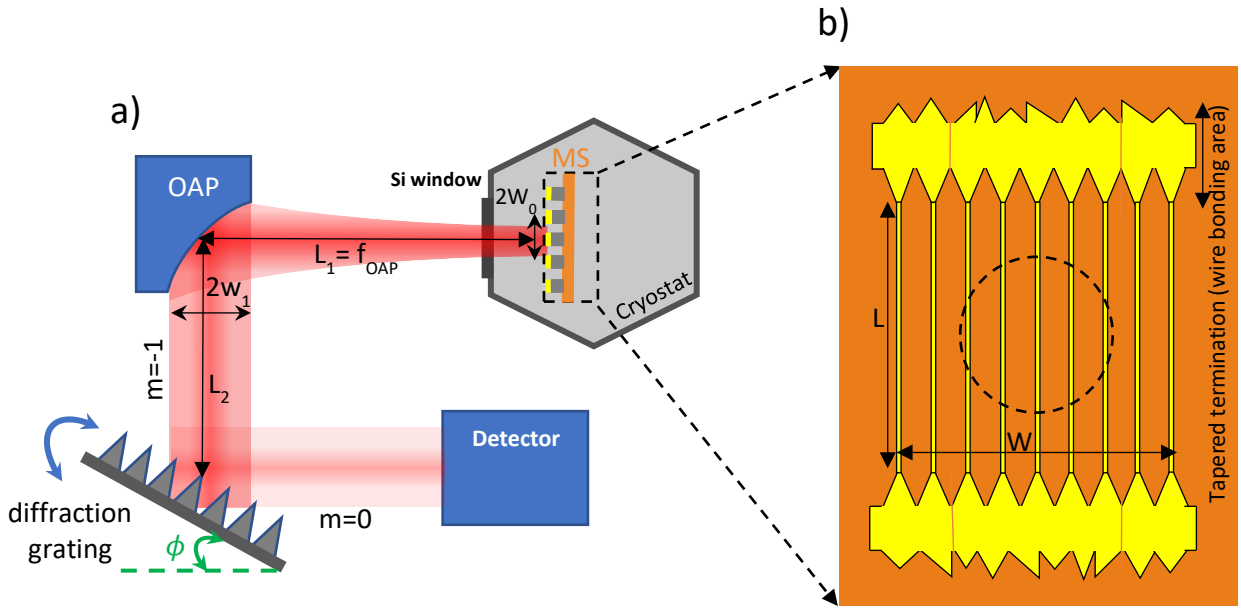

Figure 2-2: (a) Schematic of a first-order Littrow ECL based upon a large area Metasurface. Total length of the laser cavity is $L_1 + L_2$. Beam waist diameter on the metasurface is indicated by $2w_0$ and the collimated beam diameter is $2w_1$. (b) An illustration of the designed metasurface with the biased area and tapered terminations indicated. Length of the ridges is shown by L, and W is the total width of the ridges. Note that metasurface is not drawn to scale.

Using the Gaussian beam theory, we investigated several TM_{01} metasurfaces with different bias areas to estimate the collimated beam diameter and therefore the illuminated area of the diffraction grating. As mentioned in chapter 1, spectral resolution of a diffraction grating is dependent on the number of its illuminated grooves ($\frac{\Delta f}{f} = \frac{1}{mN}$). For an ideal Gaussian beam,

divergence half angle θ is wavelength dependent, and is given by $\theta = \frac{\lambda}{\pi w_0}$. Therefore, the collimated beam diameter on the OAP mirror $w_1 \approx 2 \times sin\theta \times$ focal length of OAP. To build a first-order Littrow external cavity laser as one depicted in Figure 2-2 (a), the following calculations were performed and summarized in Table 2-1. Here, we assumed that the laser beam waist radius on the metasurface is approximately equal to the bias radius. Based on the obtained results from QC-active materials, discussed in detail in chapter 3, we assumed that the laser is operating at the center frequency of 3.15 THz. Also, to satisfy the 1st-order Littrow condition at this frequency ($\lambda = \Lambda(2\sin\phi)$), diffraction grating must be placed at angle $\phi \approx 22°$.

Table 2-1: Calculated Beam parameters and spectral resolutions for the 1st-order Littrow ECL using Gaussian beam theory

Approximate size of the metasurface (length × width)	*Radius of biased area (≈ beam waist radius w_0)*	*Collimated beam diameter w_1*	*Illuminated length of the grating (= $w_1/cos\phi$)*	*Spectral resolution for m=-1 diffraction order*
6 × 6 mm^2	1.6 mm	3.8 mm	4.1 mm	97.3 GHz
4 × 4 mm^2	1.0 mm	6.2 mm	6.7 mm	59.5 GHz
2 × 2 mm^2	0.5 mm	12.3 mm	13.3 mm	30.0 GHz

In addition to modeling the laser cavity and calculating the beam parameters, we have also designed a TM_{01} metasurface, which is designed to lase at 3.15 THz, to be incorporated in our 1st-order Littrow ECL, as illustrated in Figure 2-2 (b). Therefore, a 3D unit cell of a metasurface with ridge width w = 12.5 μm and period Λ = 75 μm was simulated. Reflectance of the metasurface under normal incidence and with gain coefficient g = 40 cm^{-1} is depicted in Figure 2-3 (a). We have also plotted the change in reflectance with active medium gain g. Note that reflectance values

are drawn in log scale in Figure 2-3 (b). In this figure, g_{tr} stands for transparency gain, which will be described later (see section 2.1.1).

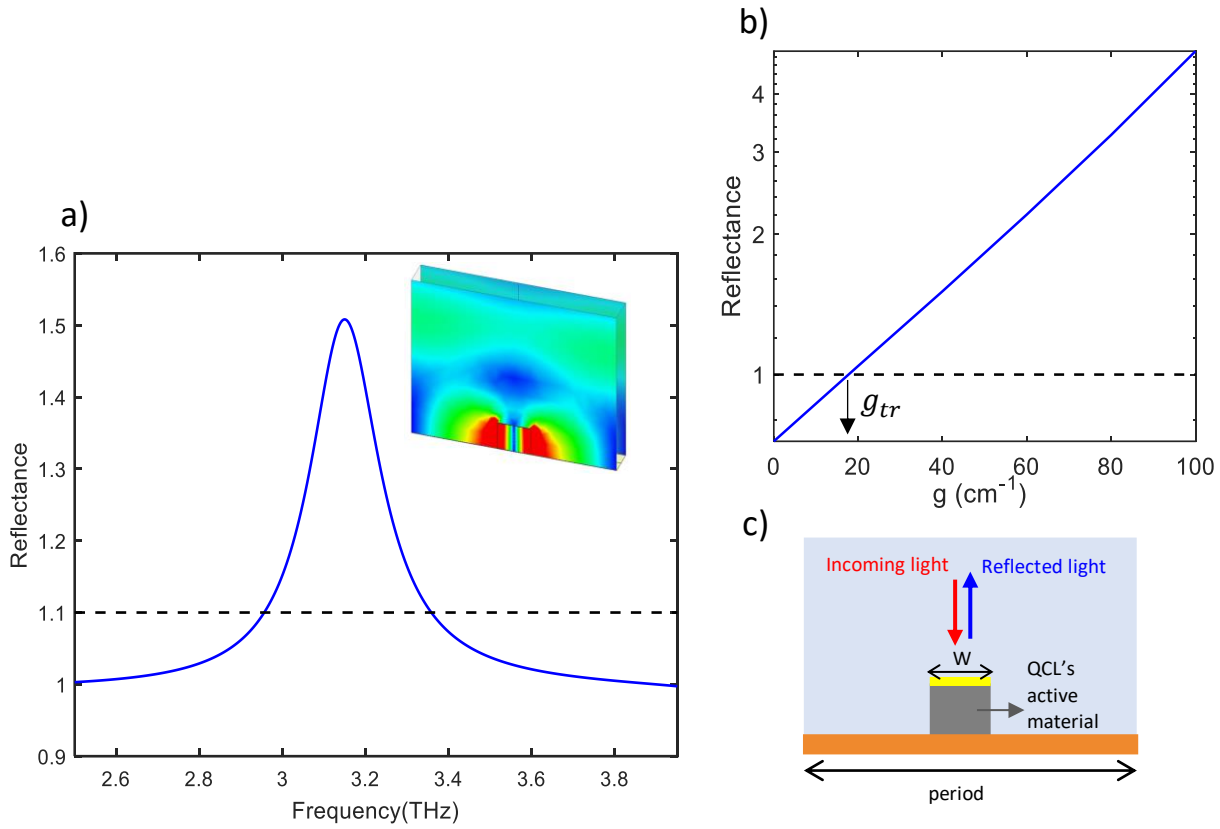

Figure 2-3: (a) Simulated reflectance spectrum for the large area metasurface with ridge width w = 12.5 μm and period Λ = 75 μm. The inset is the E-field profile for the TM_{01} mode excited under normal incidence at the resonant frequency of 3.15 THz. (b) Simulated reflectance (plotted in log scale) for different active medium gain values at the resonant frequency of 3.15 THz. In this figure, transparency gain g_{tr} = 17 cm^{-1}, and the slope of the line ξ = 3.48 × 10^{-2} cm. (c) A 2D unit cell representation of the simulated metasurface.

2.1.1 Laser model for an ideal Littrow metasurface ECL

In this section, a simple formalism is derived to describe the threshold condition for an idealized Littrow metasurface ECL. This formalism is a modified version of what is discussed for an ideal

QC-VECSEL in [19]. We consider a Littrow metasurface ECL as in Figure 2-2, where the metasurface reflector of area A has a passive reflectance R_1, the OAP mirror has reflectance R_2, and the diffraction grating has efficiency R_3 for its m=-1 diffracted order. A single-pass transmittance T for the propagation over the cavity length L is also assumed, which includes the effect of diffraction loss, atmospheric absorption, and cryostat window transmission. We can write the active metasurface reflectance R_{MS} as [19],

$$R_{MS} = R_1 G = e^{\xi(\nu)(g - g_{tr})}, \tag{2.1}$$

where $G = e^{\xi(\nu)g}$ is the reflective intensity gain at frequency ν, g_{tr} is the transparency gain coefficient of the material needed to balance absorption losses from the metal and semiconductor, and $\xi(\nu)$ is a fitting coefficient that acts as an effective propagation length and contains information about the metasurface frequency response and quality factor. We assume for the moment that the intensity is uniform in the transverse direction, and that the mode area and metasurface area are identical; later we will modify our expression to account for a transverse confinement factor. Using Equation (2.1) and requiring the intensity to be unchanged after one round trip, i.e., $|R_1 G R_2 R_3 T^2|$=1, the threshold gain coefficient g_{th} is obtained as [19]:

$$g_{th} = \frac{-\ln(T^2 R_1 R_2^2 R_3)}{\xi} \tag{2.2}$$

Equation (2.2) is in fact driven for an infinite metasurface, and ξ is obtained from simulating a unit cell of metasurface with periodic boundaries. To incorporate the effect of finite biased area of metasurface in the equation, we rewrite Equation (2.2) as

$$g_{th} = \frac{-\ln(T^2 R_1 R_2^2 R_3)}{\Gamma_t \xi}, \tag{2.3}$$

where Γ_t is the transverse confinement factor and is calculated using the equation below. However, when the transverse extent of the mode is much smaller than the biased area of the metasurface, the transverse confinement factor Γ_t approaches unity.

$$\Gamma_t = \frac{\int_{bias\ area} |\psi(x,y)|^2 dA}{\int_A |\psi(x,y)|^2 dA} \tag{2.4}$$

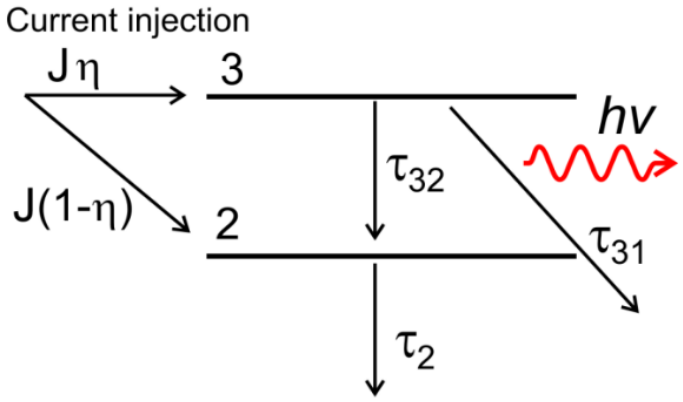

Figure 2-4: A three-level model for QC-laser active medium, where non-radiative relaxation times τ_{32}, τ_{31}, and τ_2 are shown. Level 1 (injector state) is not depicted here. Figure is taken from Ref [67].

If we model the QC- laser active material as a 3-level system, as depicted in Figure 2-4, we can also write the threshold current density as [19]:

$$J_{th} = \frac{g_{th} e L_p}{\sigma \tau_{eff}} + J_{leak}, \tag{2.5}$$

where L_p is the length of one cascade period, and $\sigma(\nu)$ is the stimulated emission cross section at the laser cavity frequency ($g(\nu) = \sigma(\nu)(n_3 - n_2)$, n_3 and n_2 are the 3D population densities of levels

3 and 2 respectively). The effective lifetime for population inversion is calculated as $\tau_{eff} = \eta\tau_{up} - (1-\eta)\tau_2$, where the effective upper-state lifetime is given by $\tau_{up} = \tau_3(1 - \frac{\tau_2}{\tau_{32}})$, and η is the injection efficiency. In Equation (2.5), J_{leak} is an empirical shunt leakage current [19].

The formalism developed above for an idealized Littrow metasurface ECL can be converted to a more common form for semiconductor lasers if we define the threshold gain g_{th} in terms of a loss coefficient α_{cav} (prorated over the cavity round trip length 2*L*) as [19]:

$$g_{th} = \frac{n\,\alpha_{cav}}{\Gamma_l} = \frac{n}{\Gamma_l}\frac{ln\,(T^2R_1R_2^2R_3)}{2L\Gamma_t}, \tag{2.6}$$

where Γ_l is the longitudinal confinement factor. In the limit of a high finesse cavity that R_1G_{th}, R_2, R_3, and T are all close to unity, Γ_l is directly proportional to the fitted ξ parameter extracted from the numerical simulations: $\xi = \frac{2L\Gamma_l}{n}$. Substituting this Γ_l into Equation (2.6), returns the original Equation (2.3). We can also write the total mode confinement factor, which describes the overlap of the mode with the QC-active material as $\Gamma = \Gamma_l\Gamma_t$. Γ can be defined using a standard expression [19],

$$\Gamma = \Gamma_l\Gamma_t = \frac{\int_{act}\varepsilon(\boldsymbol{R})|E_z(\boldsymbol{R})|^2dV}{\int_V \varepsilon(\boldsymbol{R})|E(\boldsymbol{R})|^2dV} \tag{2.7}$$

2.1.2 Modeling of external cavity by Fox-and-Li method

Fox-and-Li technique of applying Huygens integral to a wave bouncing back and forth in a cavity was first proposed with regards to maser design in 1961 [71]. Here, we use a one-dimensional version of this method to calculate the Littrow metasurface external cavity modes and

the corresponding diffraction losses. In this method an initial distribution of electric field is launched from the metasurface and propagated to the external mirror using Huygens integral, which is calculated over the finite size of the metasurface and the mirror. At each reflection, the field profile is multiplied by a spatially dependent complex reflection coefficient. The field propagates back and forth in the cavity until the mode profile and round-trip cavity loss converge to a stable solution. We represent the 1-D reflection coefficient distributions on the metasurface reflector and the external mirror by $r_{MS}(x_a)$ and $r_M(x_b)$ [69] .

$$B_n(x_b) = \sqrt{\frac{k_0}{i8\pi}} \int_{-a}^{a} A_n(x_a) r_{MS}(x_a) \frac{e^{ikR}}{\sqrt{R}} (1 + cos\theta) dx_a \tag{2.7}$$

$$A_{n+1}(x_a) = \sqrt{\frac{k_0}{i8\pi}} \int_{-b}^{b} B_n(x_b) r_M(x_b) \frac{e^{ikR}}{\sqrt{R}} (1 + cos\theta) dx_b, \tag{2.8}$$

where $A_n(x_a)$ represents the electric field distribution over the metasurface of dimension $2a$ after n round trips, and $B_n(x_b)$ is the field distribution over the mirror of dimension $2b$. In Equation (2.7) and (2.8), k_0 is the free space wave vector, R is the distance from the point x_a to x_b, and θ is the angle between the direction of the line connecting x_a to x_b and the direction of optical axis, and. After many round trips, the field in the laser cavity converges to the lowest-loss mode and the attenuation factor defined as $\gamma_n(x_a) = \frac{A_n(x_a)}{A_{n-1}(x_a)}$, calculated at an arbitrary point on the metasurface, also converges to a constant. The round-trip diffraction loss can be calculated by $2a_d = 1 - |\gamma_n(x_a)|^2$.

The described 1-D Fox-and-Li technique is applied to two laser cavity schemes: (1) a cavity formed between a metasurface, a 90-degree off-axis parabolic mirror (OAP), and a planar mirror,

as in Figure 2-2, (2) a cavity formed with a metasurface and a circular concave mirror. The first cavity models the 1st-order Littrow metasurface ECL shown in Figure 2-2 (a), and the second cavity models the 2nd-order blazed Littrow metasurface ECL depicted in Figure 2-13 (b). For the latter case, diffraction property of the metasurface is not considered, and we assume that the concave mirror is placed in front of the metasurface (perpendicular to the light propagation path) since the 2nd order diffracted beam is perpendicular to the concave mirror in the real design. To find diffraction loss in both cases, we model passive cavities with no material losses (reflectance of metasurface = 1) and PEC mirrors. Due to fabrication and material constraints, the size of metasurface is generally limited while the size of the mirrors can be much larger. Therefore, the diffraction loss is mainly induced by the mode spillover of non-vanishing tails on the metasurface edges. If we include the spatially dependent gain reflectance associated with the bias area in Fox-and-Li simulations, the change in beam size is insignificant in our models, so we use the sizes obtained from passive cavity simulations.

We first calculate the round-trip diffraction loss (in 1-D) for the 1st-order Littrow metasurface ECL using three different sizes (d_{MS}) of a metasurface. Simulations are performed at 3.15 THz, and we have assumed that a 1" diameter (d_{OM} = 1") OAP mirror with a 4" reflected focal length (RFL = 10.16 cm) and a 2" parent focal length (PFL = 5.08 cm), and a 2" diameter (d_{PM} = 2") planar mirror are placed in the laser cavity, as shown in Figure 2-5 (b). Since the OAP mirror is a segment of a parabola (in 1-D), we model its aperture as $y = \frac{(x-RFL)^2}{4\,PFL} - PFL$, where x and y axes are indicated in Figure 2-5 (b). To find the distance R between each two points on two optical components, we write the coordinates of the points on the metasurface (MS), the OAP mirror, and the planar mirror as [$-RFL, y_i^1$], [x_i^2, y_i^2], and [x_i^3, L_2], respectively,

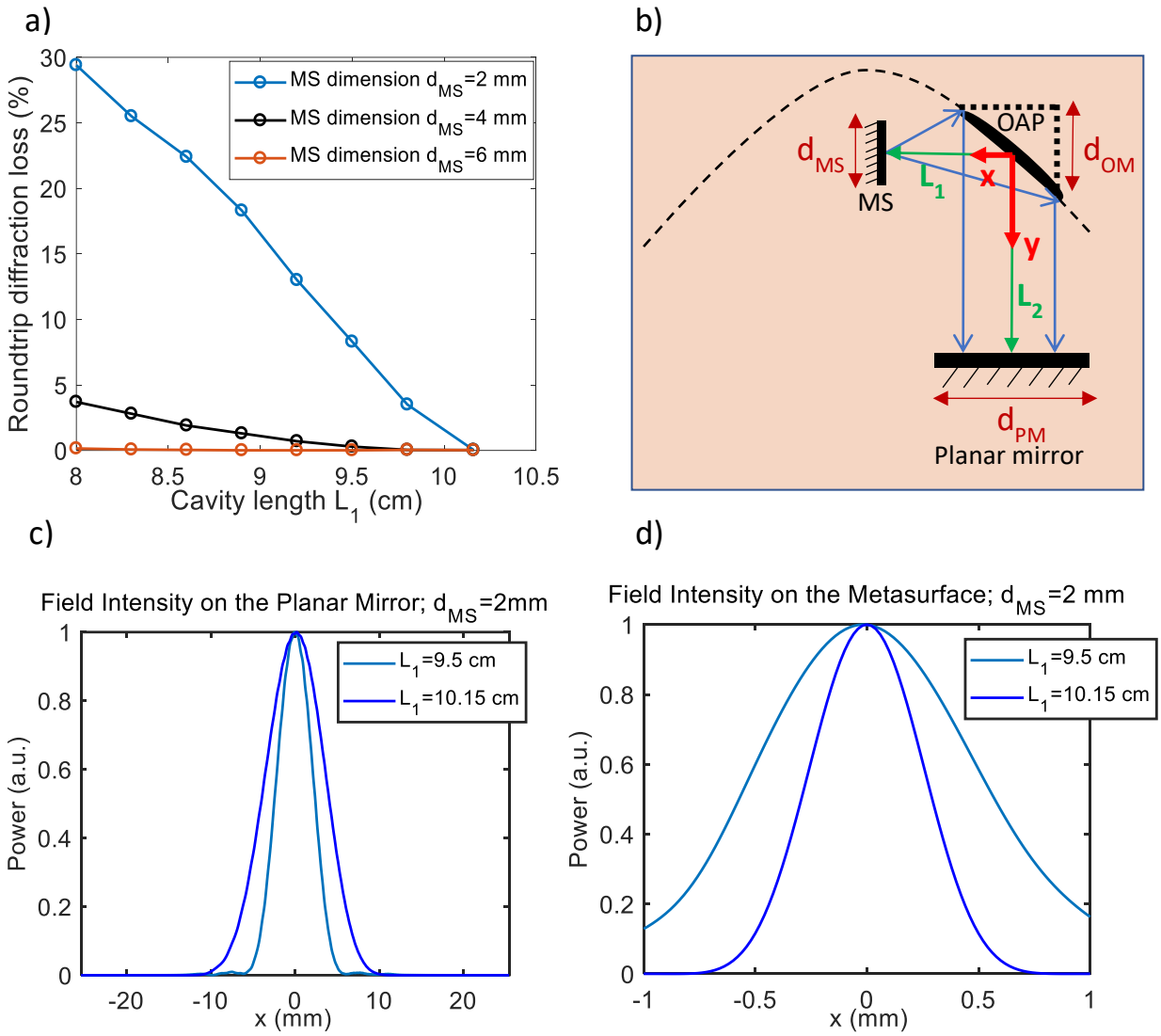

Figure 2-5: (a) Round-trip diffraction loss $2a_d$ as a function of cavity length L_1 (distance between OAP mirror and metasurface) for three different sizes of metasurface. (b) A schematic of the cavity modeled by Fox-and Li method. (c) Converged mode profiles on the metasurface for two values of L_1. (d) Converged mode profiles on the planar mirror (or diffraction grating) for two values of L_1.

where $y_i^1 \in [-\frac{d_{MS}}{2}, \frac{d_{MS}}{2}]$, $y_i^2 \in \left[-\frac{d_{OM}}{2}, \frac{d_{OM}}{2}\right]$, $x_i^3 \in \left[-\frac{d_{PM}}{2}, \frac{d_{PM}}{2}\right]$.To obtain the results plotted in these figures, I have assumed that L_2 = 8 cm (we can fit and easily move the components in the cavity as long as $L_2 >$ 5 cm, but I chose L_2 = 8 cm to push the cavity length to higher values). As

you can see in Figure 2-5 (a), diffraction losses are very small for the 4 mm and 6 mm metasurfaces, but they are significantly larger for the 2 mm metasurface. Also, as we expect, diffraction losses increase as L_1 gets shorter than the reflected focal length of OAP. The converged mode profiles on the 2 mm metasurface are also plotted for two different values of L_1 (L_1 = 10.15 cm and L_1 = 9.5 cm) in Figure 2-5 (d). Since diffraction loss for the 2mm metasurface is much smaller when L_1 = 10.15 cm compared to when L_1 = 9.5 cm, the beam waist on the metasurface is also much smaller for this case. Mode profiles on the planar mirror are also shown for the same metasurface (see Figure 2-5(c)). The beam on the planar mirror is larger when L_1 = 10.15 cm since the beam waist is smaller on the metasurface in this case, and hence the laser beam is diffracted more.

Using Fox-and-Li technique, we also calculated the round-trip diffraction loss for a laser cavity formed with a metasurface and a circular concave mirror (plano-concave cavity). In this model, we used two different sizes of a metasurface (d = 2 mm and d = 4 mm) and a 0.5”-diameter concave mirror with radius of curvature R = 50 mm. These simulations were performed at 3.3 THz to match the center frequency of operation for the blazed Littrow metasurface ECL (see section 2.2). For comparison, we also calculated the diffraction losses for a plano-plano cavity with same dimensions. This configuration is essentially an unstable cavity. However, as long as the cavity length L is small enough compared to the size of the mirrors, a near-Gaussian mode is achievable. Also, as we expect, the losses for plano-plano cavity are significantly larger than the losses in the plano-concave cavity since the latter is a considerably more stable cavity (see Figure 2-6).

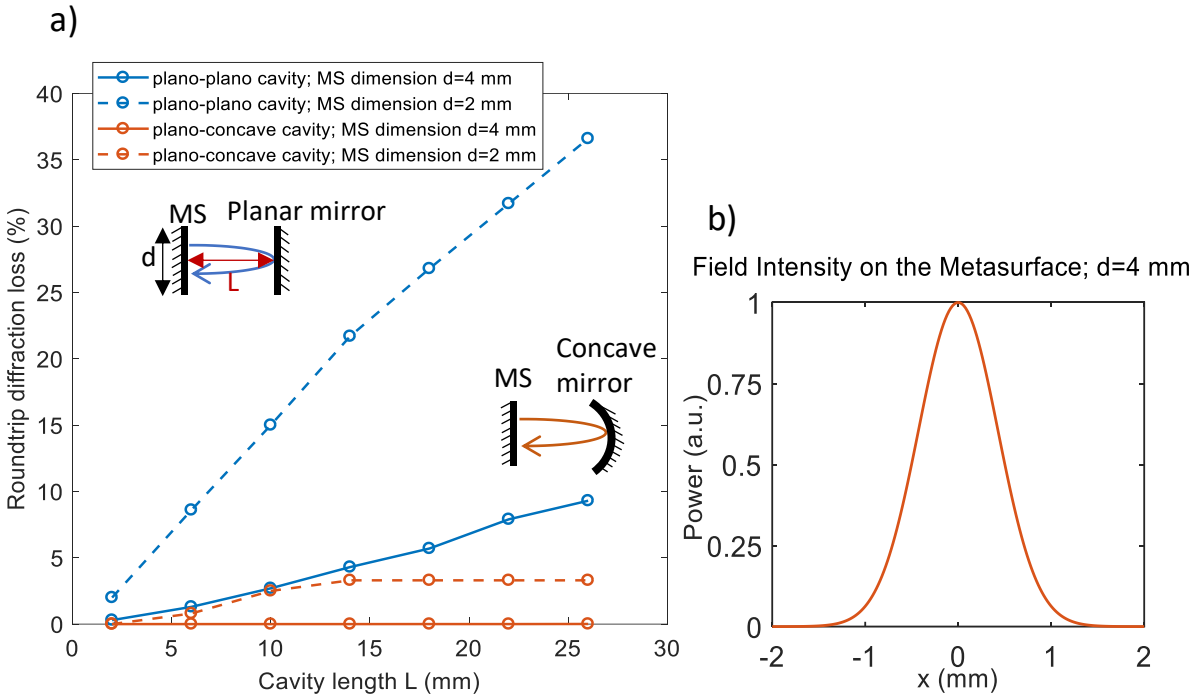

Figure 2-6: (a) Round-trip diffraction loss $2a_d$ as a function of cavity length L for a plano-plano cavity and a plano-concave cavity. Cavities are simulated for two different sizes of metasurface (d = 2 mm and d = 4 mm). A 0.5"-diamter planar mirror is utilized in the plano-plano cavities, and a 0.5"-diameter concave mirror with a 50 mm radius of curvature is used in the plano-concave cavities. (b) Converged mode profile on the 4 mm metasurface. Beam waist radius is 0.84 mm.

2.1.3 Calculation of threshold gain for the first-order Littrow metasurface ECL

Finally, the feasibility of the first-order Littrow metasurface ECL approach shown in Figure 2-2 is studied and the advantages and disadvantages of this approach for developing tunable QC metasurface lasers is discussed. In a cold Littrow metasurface ECL (i.e. QC material gain g = 0 cm^{-1}), the total cavity loss consists of (i) metasurface absorption characterized by passive metasurface reflectance R_1 or the transparency gain g_{tr}, (ii) OAP's loss determined by its reflectance R_2, (iii) Diffraction grating's efficiency for zeroth-order (out-coupling loss) determined by its first-order efficiency R_3, and (iv) external cavity loss represented by the single-pass

transmittance $T = (1 - a_a)(1 - a_w)(1 - a_d) \approx 1\text{-}a_a\text{-}a_w\text{-}a_d$, where a_a, a_w, and a_d respectively represent the single-pass power loss owing to atmospheric absorption, the absorption and reflection loss due to the cryostat window, and the single-pass external cavity diffraction loss due to cavity misalignment and metasurface finite size [69].

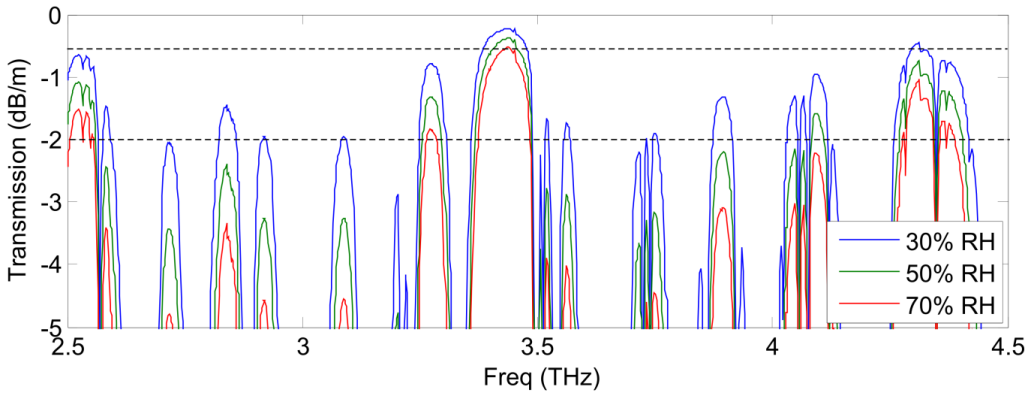

Figure 2-7: Attenuation in atmospheric transmission (in dB/m) of radiations at frequencies 2.5 THz -4.5 THz, for three relative humidity (RH) levels. Dashed lines indicate the 0.5-2 dB/m attenuation range. Figure is taken from Ref [69].

THz radiation is typically attenuated strongly by the atmospheric absorption, as shown in Figure 2-7 [69]. However, the attenuation is limited to 0.5-2 dB/m for a few transmission windows. In this range of frequencies and for a ~15-20 cm long external cavity, the single-pass atmospheric loss a_a is about 2-9%, depending on the relative humidity level and frequency. We can decrease this atmospheric loss with nitrogen (N_2) purging. In the setup shown in Figure 2-2 (a), the metasurface is mounted inside a cryostat facing the cryostat window. To eliminate reflections at the window, a high-resistivity (HR) silicon window with AR-coating must be used for the cryostat. The FTIR measured transmission of a 3.3 mm HR silicon window with anti-reflection Parylene coatings on both sides [72] is shown in Figure 2-8.We anticipate that the fringes we observe in the

measured data are some artifacts which occur because of the FTIR purging. We can match the dips in this figure with the no-transmission windows in Figure 2-7. Nonetheless, we can estimate the single-pass transmission at frequencies near 3.15 THz to be about 90%.

The round-trip diffraction loss $2a_d$ is calculated using the Fox-and-Li method explained in section 2.1.3. As shown in Figure 2-5, a_d value depends on the metasurface dimension and the length of the cavity. For a perfectly aligned cavity (L_1 = *RFL* of the OAP mirror = 10.15 cm), however, $2a_d$ is less than 0.03% (in 1-D) for all sizes of metasurface. Therefore, the roundtrip diffraction loss for the real 2-D elements is negligible (< $1\text{-}0.9997^2 \approx 0.06\%$) under perfect alignment. As mentioned before, we also solved for the stable external cavity mode using the Fox-and-Li approach, and therefore we obtained 2-D transverse confinement factors Γ_t under perfect alignment condition and somewhat imperfect alignment (L_1 = 9.5 cm) situation. The calculated Γ_t values are summarized in Table 2-2 for various sizes of metasurface and different bias radii.

As you see in Table 2-2, Γ_t reduces significantly for a 2 mm metasurface if the distance between the OAP mirror and the metasurface is less than OAP's focal length. Therefore, as expected, the 2 mm metasurface is more prone to diffraction losses. In addition to reducing diffraction losses in misaligned cavities, we can generate higher output powers if we incorporate larger metasurfaces in the 1st-order Littrow ECL. As discussed in chapter 1, widely tunable QCLs with high output powers are desirable for high-resolution spectroscopy and imaging applications.

To sum up, we can estimate the threshold bulk gain g_{th} for lasing by $g_{th}=g_{tr}-\frac{\ln(T^2R_2^2R_3)}{\Gamma_t\xi}$, using a reasonable estimate of total external cavity loss $T \approx 1\text{-}a_a\text{-}a_w\text{-}a_d$. According to our previous discussions, we obtained that atmospheric absorption loss $a_a \approx 9\%$ and the AR-coated Si window

Table 2-2: Calculated 2-D transverse confinement factors for the 1st-order Littrow metasurface ECL using Fox-and-Li technique

Metasurface dimension (mm)	*Radius of biased area (mm)*	*Distance between MS and OAP mirror (cm)*	Γ_t
6	1.6	10.15	1.0
6	1.6	9.5	0.96
4	1.0	10.15	1.0
4	1.0	9.5	0.77
2	0.5	10.15	0.94
2	0.5	9.5	0.52

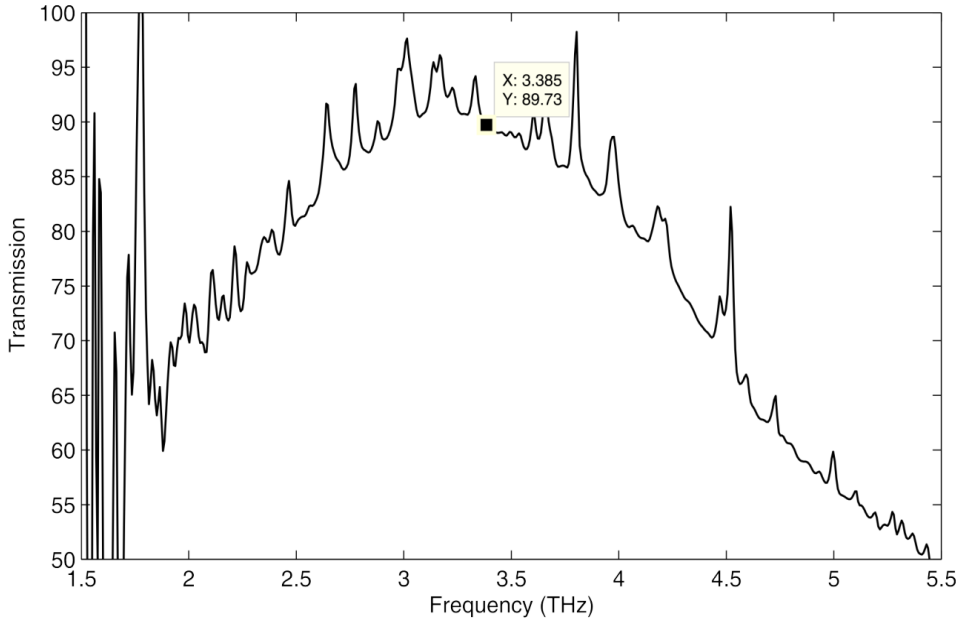

Figure 2-8: Measured transmission of a 3.3 mm HR-Si window with Parylene coatings on both sides, using FTIR. Figure is taken from Ref [72].

transmission loss $a_w \approx 10\%$. Assuming that $R_2 \approx 99\%$ for an OAP mirror with protected gold coating [73], $R_3 \approx 90\%$ (for the previously described diffraction grating) at 3.15 THz (see Figure 1-3), g_{tr} = 17 cm^{-1}, and $\xi = 3.48 \times 10^{-2}$ cm (= slope of the line in Figure 2-3 (b)), we can obtain

g_{th} values for the metasurfaces listed in Table 2-2, based on their Γ_t and a_d values obtained from Table 2-2 and Figure 2-5, respectively.

Threshold gain g_{th} values calculated for the 1st-order Littrow metasurface ECL are summarized in Table 2-3, and are compared with the threshold gain we have calculated for the conventional intra-cryostat QC-VECSEL described in section 1.5. A 2×2 mm^2 metasurface was used in this VECSEL, but only a center circular area of 1 mm diameter was biased. Metal-metal ridges were 11.5 μm wide and period Λ of metasurface was 70 μm. To get g_{th}, we obtained g_{tr} = 17 cm^{-1} and ξ = 1.63 × 10^{-2} cm from HFSS simulations, and we calculated the 2-D roundtrip diffraction loss $2a_d$ = 4.7% and the 2-D confinement factors Γ_t = 57%, using Fox-and-Li model for the plano-plano cavity. We also assumed that we're using a low reflectivity output coupler R_2=90% to match the diffraction grating efficiency we considered previously. We should note that the atmospheric absorption loss and window transmission loss are both zero in this case since this VECSEL was entirely mounted in the dewar.

As we see in Table 2-3, g_{th} values for the perfectly aligned 1st-order Littrow metasurface ECL are close to the threshold gain value for a conventional QC-VECSEL. In fact, these values are a little smaller than the threshold gain of a conventional VECSEL since the confinement factor is larger and the diffraction loss is lower if we use focusing optics instead of a flat output coupler. For larger area metasurfaces (4 mm and 6 mm metasurfaces), threshold gain coefficients remain close to the gain value of the conventional VECSEL even under misaligned cavity conditions. However, g_{th} value significantly increases for a 2 mm metasurface if the distance between the OAP mirror and the metasurface is less than OAP's focal length. It is, therefore, easier to achieve lasing in the 1st-order Littrow metasurface ECL if a larger area metasurface is utilized compared

to the 2 mm metasurface, especially in a misaligned cavity. We believe that these levels of bulk gain (g_{th} ≈ 33-38 cm^{-1}) are achievable by QC materials. Therefore, it is feasible to develop a tunable QCL using the proposed 1st-order Littrow metasurface ECL setup with a larger area metasurface.

Table 2-3: Calculated threshold gain values for the 1st-order Littrow metasurface ECL and a typical QC-VECSEL

Metasurface dimension (mm)	*Radius of biased area (mm)*	*Distance between MS and OAP mirror (cm)*	g_{th} *(cm^{-1})*
6	1.6	10.15	32.8
6	1.6	9.5	33.4
4	1.0	10.15	32.8
4	1.0	9.5	38.0
2	0.5	10.15	33.8
2	0.5	9.5	58.7
Comparison with a conventional QC-VECSEL			
Metasurface dimension (mm)	*Radius of biased area (mm)*	*Cavity length (mm)*	g_{th} *(cm^{-1})*
2	0.5	2.5	33.5

To make the lasing even less challenging and to lower the required gain for this type of lasers, several strategies could be considered and implemented in future. First, we can improve the transmission of the cryostat window by reducing the loss in the AR-coated window. Instead of using Parylene, we can micromachine an artificial dielectric as a quarter wave transformer on both sides of the Si wafer [74]. This way, we can increase the transmission of the window up to 96% and reduce the threshold gain to 28.6 cm^{-1} (for the 6 mm metasurface and 10.15 cm long cavity). Also, we can increase the confinement factor Γ_t by using larger area devices so that even a misaligned cavity would not hinder the laser operation. However, to reduce the power consumption and to allow CW operation for these larger area metasurfaces, we must design new metasurfaces.

We can, for example, use patch antennas instead of ridges to reduce the heat dissipation density. And lastly, we might be able to improve the first-order efficiency of our diffraction grating by purchasing a customized grating in the future.

For the reasons stated above, we designed two metasurfaces with the same ridge width and period (w = 12.5 μm and Λ = 75 μm), but different bias areas and therefore different metasurface areas. An illustration of the metasurface with the bias area and tapered terminations is shown in Figure 2-2. In one of the designs, length of the ridges L is ~6.4 mm, total width of the ridges W is ~6.3 mm, and bias radius is 1.6 mm. For the other design, the bias radius = 1.0 mm, L = 4 mm, and $W \approx$ 3.9 mm. We should note that these metasurfaces have very large bias areas. Therefore, their power consumption is very high, and it is very important to have a proper heat sink. Also, to increase the loss for TEM_{00} mode along the ridges and to make sure that self-lasing is suppressed, an irregular random tapered area was designed for these metasurfaces (as depicted in Figure 2-2 (b)). The middle part in the tapered termination area is also electrically disconnected from the two side areas so that we are certain that only the middle ridges are biased in case of oxide failure.

Table 2-4: Calculated spectral resolutions for the 1st-order Littrow ECL using Fox-and-Li approach

Metasurface dimension (mm)	*Radius of bias area (mm)*	*Beam waist radius on the metasurface (mm)*	*Beam waist radius on planar mirror (or diffraction grating) (mm)*	*Spectral resolution for m=-1 order (GHz)*
6	1.6	0.48	6.63	30.1
4	1.0	0.48	6.63	30.1
2	0.5	0.48	6.73	29.6

We also recalculated the grating spectral resolutions using Fox-and-Li method for those three sizes of metasurface and under perfect alignment (length of cavity = focal length of OAP)

condition. We should note that a planar mirror was used in the place of the diffraction grating in Fox-and-Li simulations, but now we can assume that planar mirror was in fact a diffraction grating to obtain spectral resolutions. According to the calculations presented in Table 2-4, the focused laser beam is 0.96 mm wide on the metasurface, in all cases, and therefore the spectral resolution is about 30 GHz. Another important thing that we can notice in the above table is that beam waist radius is much smaller than the radii of bias areas (for 4 mm and 6 mm devices). This means that a large portion of the gain, and thus a lot of current, that is provided by a metasurface with a large bias area will be wasted. This is, however, the price to pay for having more tolerance for misalignment.

Assuming that total length of laser cavity ($L_c = L_1 + L_2$) is about 18 cm, the free spectral range (FSR) of the laser is given by $\text{FSR} = \frac{c}{2nL_c} \cong 830$ MHz. Therefore, by incorporating the described metasurfaces in our Littrow metasurface ECL, we will have a multi-mode tunable laser since the spectral resolution is larger than FSR, but less than the gain-bandwidth (resolution $\approx 36 \times$ FSR). As shown in the electromagnetic simulations of this metasurface in Figure 2-3, the gain-bandwidth is about 400 GHz. We can treat the diffraction grating as a reflector with a Lorentizan reflection function R_g, for which FWHM = grating's spectral resolution, to illustrate the relationship between the spectral resolution of the grating, FSR of the cavity, and the metasurface gain-bandwidth (see Figure 2-9).

At first glance, we might think that the laser beam on the grating must have been 30 times larger than what it is now to achieve single mode operation. It is extremely difficult, if not

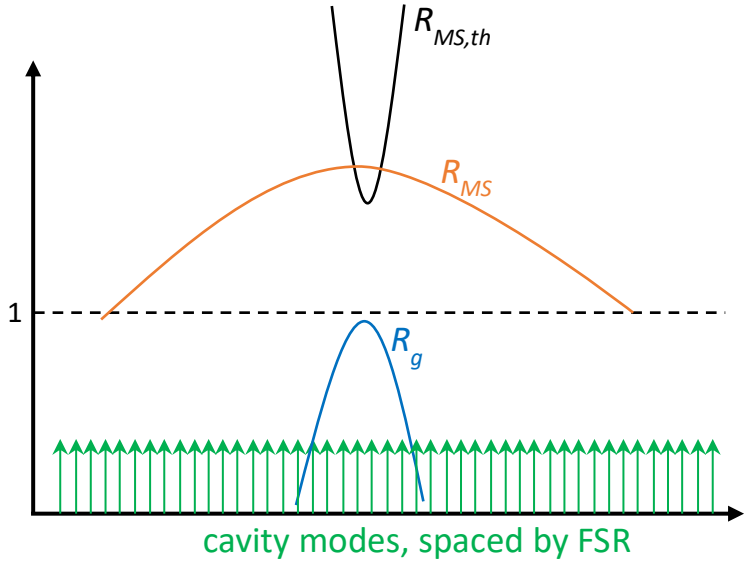

Figure 2-9: Reflectance of the metasurface, reflectance of the diffraction grating, and cavity modes that are spaced by FSR are shown to illustrate the filtering effect of the grating. The threshold reflectance gain from the metasurface $R_{MS,th}$ is inversely proportional to R_g, and therefore, its FWHM is smaller than FWHM of R_g.

impossible, to enlarge the beam this much without scaling the cavity length, even if we use different optics (an OAP with different focal length or using a concave mirror instead of an OAP mirror). But in fact, things are a little more favorable since the threshold reflectance gain from the metasurface $R_{MS,th}$ will be inversely proportional to R_g ($R_{MS,th}$=($R_g R_2{}^2 T^2$)$^{-1}$). The inverse behavior will lead to a very fast change in the required threshold, and effectively a much more selective filtering effect. Additionally, if we are dealing with a homogeneously broadened gain, we will end up with a single mode laser even if the spectral resolution is much broader than FSR. Because in this case, only the mode that is closest to peak of the gain and has the highest gain-to-loss ratio will lase. There are evidences in typical QC-metasurfaces that indicate that gain is homogeneously or quasi-homogenously broadened. For conventional QC-VECSELs, the gain bandwidths are

typically a few hundreds of GHz and FSR's are usually below 75 GHz, however, we have mostly observed single mode lasing to date (occasionally observed dual mode lasing, especially during the mode hop, and once we saw 4 modes in a broadband metasurface).

Therefore, the 1st-order Littrow metasurface ECL proposed in this thesis can provide single mode, broadband tuning (~ 400 GHz) if the total gain from the metasurface and the active material is homogeneously broadened. Also, compared to the 2nd-order blazed Littrow metasurface ECL discussed in the next section, the 1st-order Littrow metasurface ECL must deal with less space constraints since all the external optical components are placed outside of the cryostat. Consequently, optical alignments are also easier to modify once the metasurface is mounted and cryostat is closed. Furthermore, we can use this setup for other type of experiments such as laser feedback interferometry [75] by merely replacing the diffraction grating by another target. This interferometry technique has many applications in sensing and imaging, including the measurement of internal laser characteristics, trace gas detection, materials analysis, and biomedical imaging [75].

Although 1st-order Littrow metasurface ECL approach has many advantages, there are several drawbacks that can limit their practicality and applications. First, the output beam (specular reflection) will be steering as we rotate the grating, and therefore, it will be difficult to collect the output without an additional compensating mirror. Secondly, even though it seems that enough gain is provided by the metasurface to overcome the losses in the laser cavity, the losses are still considerable, and in practice the losses could be even larger than anticipated. For instance, the 90% efficiency that we used for our diffraction grating was only an estimate based on a general efficiency curve that was given in [29] for a sawtooth grating with a blaze angle of 26°45'.

However, as discussed in chapter one, efficiency depends, along with other factors, on the use conditions and the coating material, and we never measured the actual efficiency for our specific diffraction grating. Also, diffraction losses can be significantly larger if misalignments are worse than what I have considered here. The last problem with this approach arises from the fact that the 1st-order Littrow metasurface ECL could potentially result in a multi-mode laser with a broad linewidth and therefore, its application is limited to absorption spectroscopy of solid-state materials and multi-spectral imaging. The proposed laser will not be suitable for heterodyne spectroscopy applications and absorption spectroscopy of trace gases.

2.2 Blazed Littrow metasurface ECL

Conventional optical components such as lenses and diffraction gratings can shape the wavefront of light and provide considerable changes in amplitude, phase, and polarization of light only when the light beam has propagated over distances much larger than the wavelength. In contrast, a metasurface is a two-dimensional surface (with a thin thickness) that can provide abrupt changes in the optical properties of a light beam by adjusting the transmission/reflection properties of its surface [76]. It has been shown in recent years that a blazed metasurface grating, operating at microwave frequencies, can mimic the operation of a typical sawtooth right-angle grating [77]. The non-planar sawtooth structure can be replaced with an equivalent planar metasurface which has particular reflection phase regions across its surface. The metasurface provides tangential surface currents that create the same scattered field as the non-planar sawtooth grating.

To develop high-efficiency blazed gratings that operate at a particular incident angle and frequency, a simpler approach than the one used in [77] can be implemented. It has been demonstrated by the same group that planar periodic structures which have a single resonator on a

grounded dielectric substrate in their unit cell can provide perfect blazing or perfect auto-collimation [78]. Typical right-angle sawtooth gratings are only capable of modest levels of blazing. Meaning, some amount of the incident energy always goes to the specular reflection, and thus the wave is not completely retroreflected. However, perfect blazing (m=-1 diffraction order has 100% efficiency) has been previously demonstrated using groove-based gratings [79], strip gratings on thick grounded dielectric slabs [80], and dielectric rod-based gratings [81]. The common feature that enables perfect blazing in all these structures is the strong coupling between the incident wave and a resonance in the unit-cell. This idea of resonator-based gratings can be extended to structures which have multiple coupled resonators per unit cell to provide a wide range of operating frequencies and angles. In order to design a grating, which provides perfect blazing for a bandwidth of frequencies and incident angles, the period of the structure must be determined by the Bragg condition (Equation (1.1)), and the width of the resonators and the spacing between them must be optimized to achieve the highest amount of rejection for the specular reflection [70].

2.2.1 Modeling of blazed metasurface gratings

Inspired from these works at microwave frequencies, we figured that we can implement this technique in THz QC-metasurfaces and integrate the functionality of a diffraction grating into the quantum-cascade amplifying metasurface. This novel idea was first proposed by Tatsuo Itoh and Mohammad Memarian, and it was studied more extensively by the author of this thesis. Here, we have engineered active metasurface gratings that are designed for "blazing" on either the 1st or 2nd diffraction orders. These metasurface gratings can be incorporated in a laser cavity to develop Littrow ECLs. Figure 2-1 (b) demonstrates the 1st-order blazed Littrow metasurface ECL, which consists of a blazed metasurface grating and a concave mirror and is fully constructed within a

cryostat. In this case, the steering zeroth order (specular) beam will be collected as the output of the laser. In contrast, the 1st-order beam which is free from beam scanning with tuning will be the output in the 2nd-order blazed Littrow metasurface ECL scheme, as shown in Figure 2-1 (c). If we impose the Littrow condition on *m*=-2, we will find the following condition on the period Λ of the metasurface grating using Equation (1.1):

$$\sin\theta_i + \sin\theta_{-2} = -2\frac{\lambda}{\Lambda}$$
$$\sin\theta_i = \sin\theta_{-2}$$
$$\Lambda = \frac{-\lambda}{\sin\theta_i}$$

This period causes the *m*=-1 angle to be zero, independent of wavelength and incident angle:

$$\sin\theta_i + \sin\theta_{-1} = -\frac{\lambda}{\Lambda}$$
$$\sin\theta_{-1} = -\frac{\lambda}{\Lambda} - \sin\theta_i = -\frac{\lambda}{\Lambda} - (-\frac{\lambda}{\Lambda}) = 0$$

To keep *m*=+1 or *m*=-3 evanescent, Λ must satisfy:

$$\sin\theta_{+1} = 2\frac{\lambda}{\Lambda} > 1 \rightarrow \Lambda < 2\lambda$$
$$\sin\theta_{+3} = -2\frac{\lambda}{\Lambda} < -1 \rightarrow \Lambda < 2\lambda$$

The described metasurface gratings are designed using a coupled-resonator approach, where 2 or 3 inhomogeneous antennas are coupled within a unit cell. This allows Littrow "blazing" to be engineered, so that the majority of incident power is retroreflected into either the *m*=-1 or *m*=-2 diffractive order, while scattering into other orders is suppressed. Full-wave EM simulations of the reflectance for such a 1st-order and a 2nd-order blazed metasurface are shown in Figure 2-10 and Figure 2-11, respectively. As the simulated frequency is changed, the incident angle of the light is also varied according to the grating Equation (1.1). Also, as in previous simulations, when QC-gain is applied to the metasurface, the reflectance increases above unity. Gain bandwidth (also

tuning range) is about 400 GHz for the 1st-order blazed metasurface grating and about 340 GHz for the 2nd-order blazed metasurface.

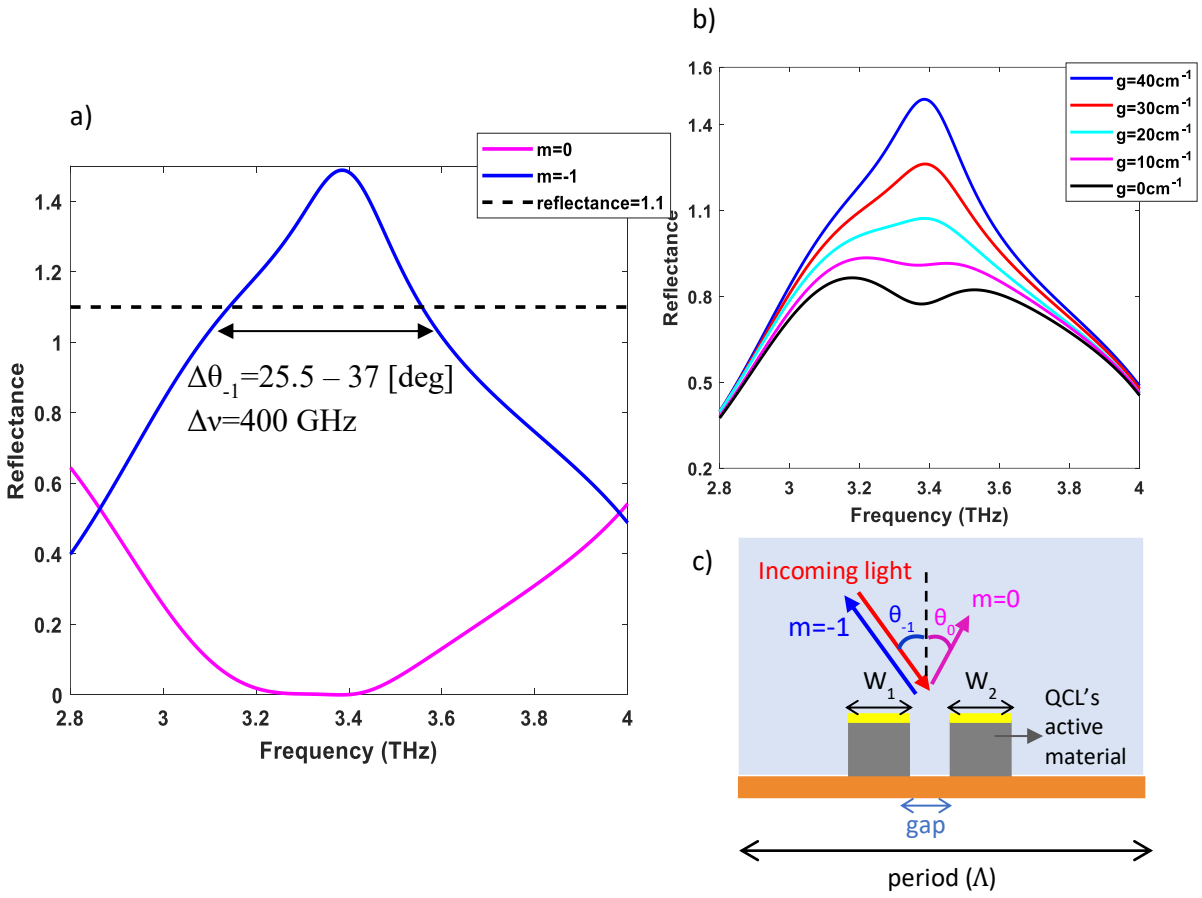

Figure 2-10: Electromagnetic simulations for the 1st-order blazed Littrow metasurface ECL. (a) Reflectance spectra for zeroth order (specular reflection) and 1st order diffracted beams. (b) 1st-order diffraction spectra for different QC gain values. c) A 2D unit cell representation of the 1st-order blazed metasurface grating with w_1 = 11 μm, w_2 = 13 μm, Λ = 88.5 μm.

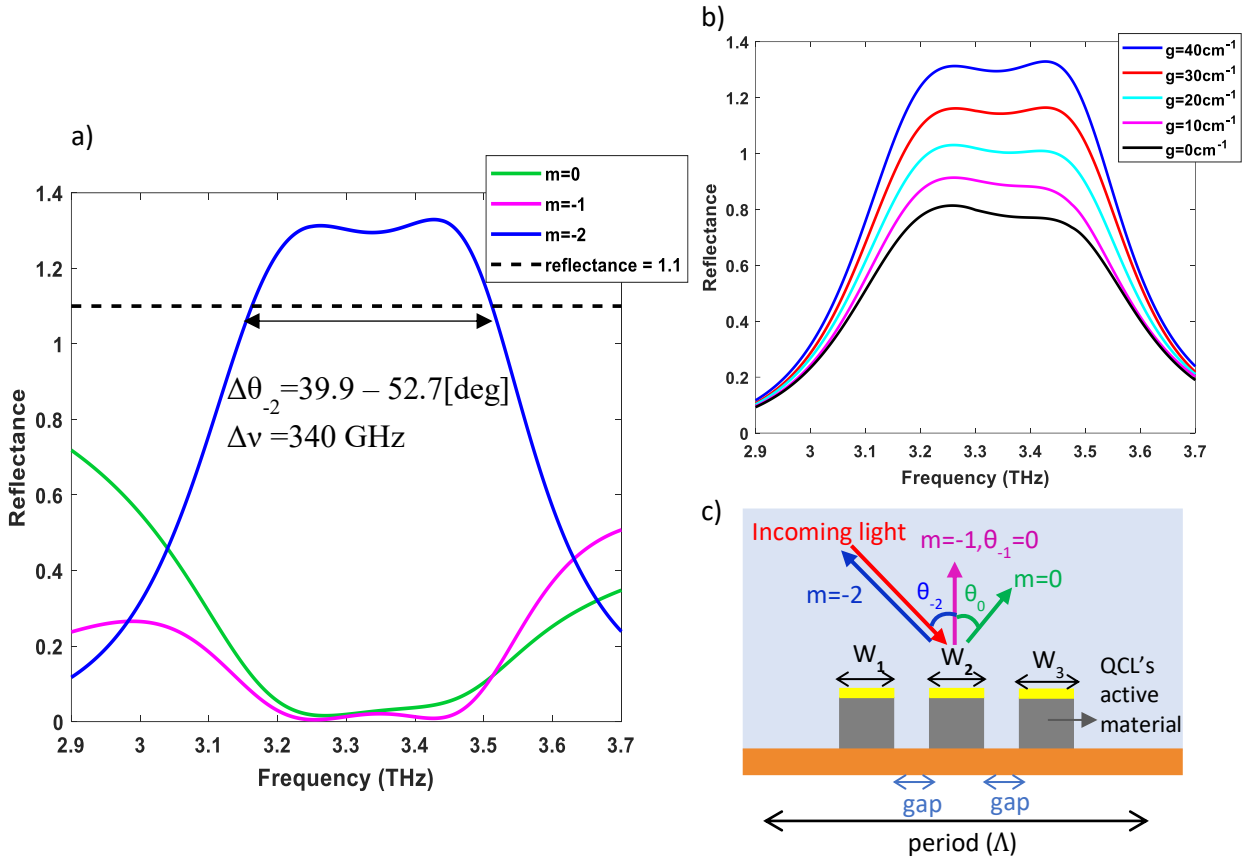

Figure 2-11: Electromagnetic simulations for the 2nd-order blazed Littrow metasurface ECL. (a) Reflectance spectra for zeroth order (specular reflection), 1st, and 2nd order diffracted beams. (b) 2nd order diffraction spectra for different QC gain values. (c) A 2D unit cell representation of blazed metasurface grating with w_1=10.5 μm, w_2=11.7 μm, w_3=13 μm, Λ = 130 μm.

2.2.2 Stability analysis for blazed Littrow metasurface external cavities

Comparing the two designs presented in the previous section, the Littrow ECL based upon 2nd-order blazed metasurface grating is the better scheme for developing tunable QCLs since the output beam will be taken from the *m*=-1 diffraction order in this case and will not steer as the laser is tuned. This is highly desirable for most applications. Also, as we see in the simulations,

the gain is flatter across the tuning range for the 2nd-order blazed metasurface. This means that all frequencies (modes) will experience the same gain and will therefore have similar beam shapes.

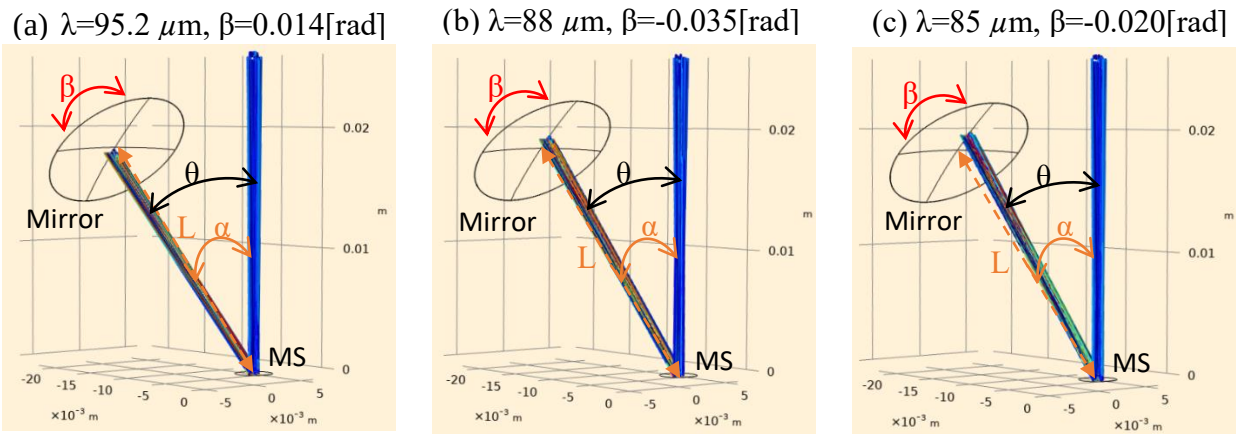

Figure 2-12: Ray tracing analysis for the 2nd-order blazed Littrow metasurface ECL. (a) For λ = 95.2 μm, 0.8°(0.014 rad) rotation of concave mirror is needed to maintain a stable laser cavity. (b) For λ = 88 μm, the concave mirror must be rotated -2.0°(-0.035 rad) to keep the external cavity stable. (c) For λ = 85 μm, -1.1°(0.020 rad) rotation of concave mirror is needed for a stable cavity.

We have performed ray-tracing analysis to ensure the stability of the 2nd-order blazed Littrow metasurface ECL. In contrast to Fox-and-Li method, we can incorporate the grating property into the metasurface here and model the real three-dimensional cavity. In these simulations, period of metasurface grating (MS) is 130 μm, as the case in Figure 2-11, L = 25.7 mm, radius of curvature R = 50 mm, diameter of mirror D = 12.7 mm. These values are chosen for the reasons explained in the next section. The concave mirror is placed at the fixed angle α = 45° with respect to the metasurface. The second order diffracted rays leave the metasurface with angle $\theta = \arcsin(2\lambda/2\Lambda)$, according to the general grating equation. Therefore, the concave mirror is rotated around its own central axis to maintain the stability of the cavity (see Figure 2-12). We

made sure that after 10000 passes, rays still retrace themselves and remain inside the structure. Simulations are performed for frequencies 3.15 THz, 3.4 THz, and 3.5 THz (all included in the gain-bandwidth of the 2nd-order blazed metasurface grating). Note that only m=-2 and m=-1 diffraction orders are drawn in the figures.

2.2.3 Design of intra-cryostat blazed Littrow metasurface external cavity

To build the 2nd-order blazed Littrow metasurface ECL, as depicted in Figure 2-13, entirely within the cryostat, the following stages and optics were chosen to meet the size constraints. A piezoelectric rotator (ANR240/RES/LT) was purchased from Autocube Systems AG [82] to be used in our small-size homemade optical system under high vacuum and at temperatures as low as 4 Kelvin. This rotator can provide full 360-degree rotation with steps of 10^{-3} degree. Also, a concave mirror with diameter d = 0.5" [83] was purchased to be mounted on top of the piezoelectric rotator [84]. We also performed Fox-and-Li simulations for different cavity lengths and radii of curvature to obtain the beam waists on the metasurface and therefore the spectral resolutions under various conditions. From these calculations, which are summarized in Table 2-5, we figured out that a ~4 mm metasurface with a ~2mm bias diameter must be used in order to confine the laser beam in the biased area. To perform these simulations, we assumed that center lasing frequency is at 3.3 THz (see Figure 2-11).

Since spectral resolutions were almost similar between the four designs, a concave mirror with a 50 mm radius of curvature was selected and the cavity length was designed to be about 25 mm to meet the space constraints imposed by the cryostat. Consequently, with these choices, the free spectral range (FSR) for the 2nd-order blazed Littrow metasurface ECL will be ~6 GHz. Also, since the concave mirror is placed at 45° angle with respect to the metasurface, an elliptical laser

beam will be formed in the cavity. Therefore, to ensure that the spot size on the metasurface is less than or equal to the biased area, a metasurface with an elliptical biased area of diameters 2 mm × 2.8 mm was designed.

Table 2-5: Calculated beam parameters and resolution for the blazed 2nd-order Littrow metasurface ECL

Radius of curvature of concave mirror (mm)	*Distance between MS and mirror (mm)*	*Beam waist radius on the MS (mm)*	*Beam waist radius on the Mirror (mm)*	*Spectral resolution (GHz)*
R = 50	25	0.84	1.17	127.7
R = 50	15	0.80	0.97	134.1
R = 100	50	1.22	1.65	87.9
R = 100	15	1.00	1.09	107.3

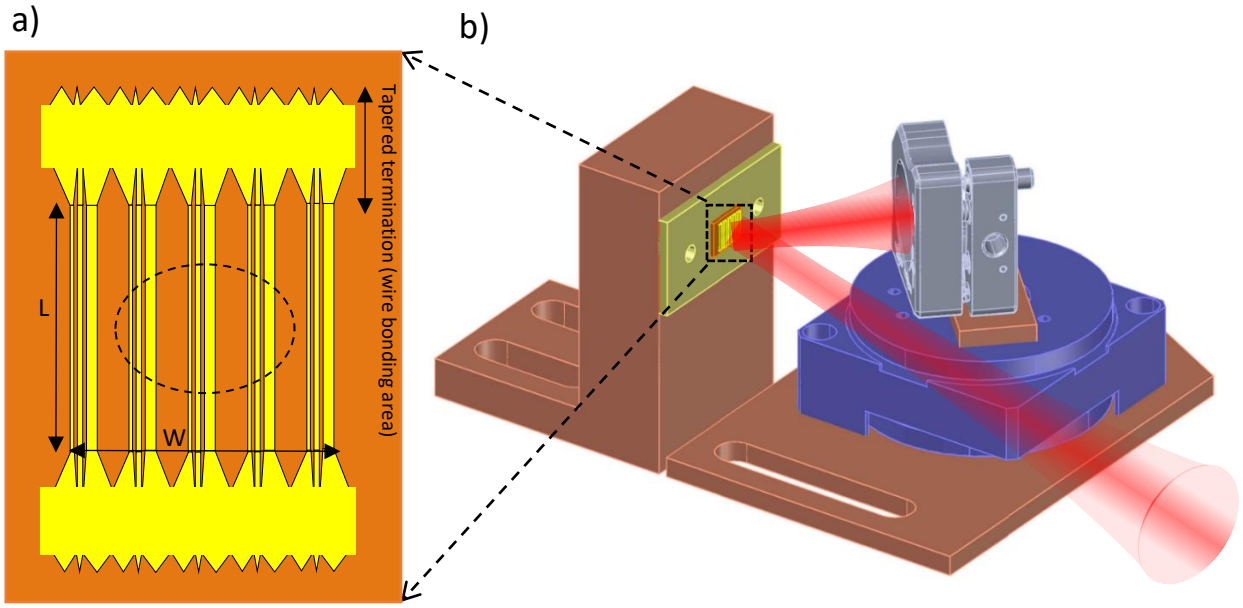

Figure 2-13: (a) An illustration of the designed 2nd-order blazed metasurface grating with the biased area and tapered terminations indicated, with L = 4.3 mm and W = 4.2 mm. Metasurface is not drawn to scale. (b) Schematic of a 2nd-order blazed Littrow metasurface ECL, designed to be mounted inside our cryostat. Drawings of piezo-rotator and the mirror's mount are taken from [82] and [84] respectively.

We can follow the same procedure as in section 2.1.3 to estimate the threshold gain for the laser shown in Figure 2-13 (b). If we estimate the single-pass transmission $T \approx 100\%$ (since the atmospheric absorption loss, the cryostat window loss, the diffraction loss are all zero), $R_2 \approx 99\%$ for the gold-coated concave mirror [73], $\Gamma_t \approx 96\%$, $g_{tr} = 17$ cm^{-1}, and $\xi = 1.24 \times 10^{-2}$ cm, we obtain $g_{th} = g_{tr} - \frac{\ln(T^2 R_2)}{\Gamma_t \xi} = 17.8$ cm^{-1}. This level of gain is easily achievable for QC materials (compare it with the threshold gain value for the conventional QC-VECSEL in Table 2-3). Therefore, it is feasible to implement this tunable laser. In fact, it is much easier to obtain lasing in this cavity compared to the 1st-order Littrow metasurface ECL.

We should note here that we could have also implemented the cavity shown in Figure 2-13 (b) outside of the cryostat and possibly over a longer propagation path. However, geometry of the cavity would have been more complex and it would have been more difficult to align the optical components for several reasons: (1) the blazed metasurface must be mounted in such a way that the 45° 2nd-order beam and the 1st-order beam could both go through the cryostat window, (2) the metasurface that is placed within the cryostat must be perfectly aligned with the concave mirror which is outside of cryostat and is mounted on a separate mount. Therefore, it is reasonable to consider constructing this cavity only within the cryostat. To align the intra-cryostat laser cavity, depicted in Figure 2-13, we can mount the whole structure on a single large plate, align the metasurface and the concave mirror using a He:Ne laser, and then attach that plate to the cold stage of a dewar. To align the metasurface and the mirror, we should first align the He:Ne laser with the metasurface to make sure they're parallel to each other. Then, we rotate the He:Ne laser and place it at 45° angle with respect to the metasurface while preserving the parallelism. Now, using the

two adjusters on the kinematic mirror's mount, the mirror is adjusted until it is perpendicular to the laser beam. In this case, the laser beam will retrace itself.

Similar to the previous 1st-order Littrow metasurface ECL, the proposed 2nd-order blazed metasurface ECL has a spectral resolution (~120 GHz) which is larger than its FSR (~6 GHz). Therefore, we expect this laser to be a multi-mode laser too, unless the total gain from the metasurface and the active material is homogeneously broadened. In fact, things are a little more favorable in this case since the spectral resolution $\approx 20 \times$ FSR (in contrast to $36 \times$ FSR). Nonetheless, this multi-mode laser (with a broad linewidth) will be only suitable for absorption spectroscopy of solid-state materials and multi-spectral imaging. To decrease the chance of a multi-mode behavior in alternative designs in future, the spectral resolution must be reduced by increasing the number of illuminated resonators (grooves). This can be done by re-designing the metasurface grating with a smaller period and/or by using concave mirrors with larger radii of curvature. Denser metasurfaces or larger area metasurfaces, however, will have larger power consumptions and larger heat dissipations, and therefore, CW operation would be prevented. To reduce current draw in dense and large metasurface gratings, other novel metasurface designs must be pursued.

Another problem with this approach comes from the fact that the efficiency of the blazed metasurface grating for m=-1 diffracted beam (output of laser) is unknown. Simulations show that m=-1 diffracted order will have a very small power, but it is unknown if this small value would be easily detectable in practice or not. However, compared to the case in Figure 2-2, the output beam will be fixed as we tune the laser, so it will be much easier to detect the output if there's enough optical power.

Chapter 3: QC ridge and VECSEL fabrication and measurements

As discussed previously, broadband QC gain material is a critical component for realizing tunable QC lasers. This project started with five new 4" GaAs wafers with MBE grown QCL heterostructures. The wafers were provided by Dr. John Reno of Sandia National Laboratories and Northrop Grumman. These wafers were first processed into metal-metal waveguide lasers so their lasing characteristics (power consumption, output power, emission frequency, and temperature performance) could be determined. QC active metasurfaces and metasurface gratings presented in chapter 2 were designed based on the collected data from theses MM waveguides. In this chapter, I will provide some details on the active region designs, describe the fabrication process and the experimental setup, and present the results of tested devices.

3.1 QC active material design

THz QCLs are typically constructed using GaAs/$Al_xGa_{1-x}As$ material systems that are grown by molecular-beam epitaxy (MBE). Figure 3-1 shows a typical band diagram for a four-well hybrid resonant-phonon QCL design. The figure illustrates two cascaded modules, each including four quantum wells. But in real growths, QC active materials typically consist of hundreds of these modules. When the modules are properly biased, the sub-bands in the wells line up to allow electron transport. The hybrid resonant-phonon design benefits from a diagonal optical transition (like in a bound-to-continuum active region) and a phonon-assisted depopulation scheme (similar to a resonant-phonon design). In the resonant-phonon scheme, the lower radiative state 1 is brought

into a broad tunneling resonance with the excited state in the adjacent quantum wells, so that its wavefunction maintains a strong spatial overlap with the injector states over several quantum wells, whereas the upper lasing state 2 remains localized and has very little overlap with the injector states. Therefore, the lower radiative state can experience sub-picosecond LO-phonon scattering time, while the upper state preserves a lifetime of several picoseconds [1].

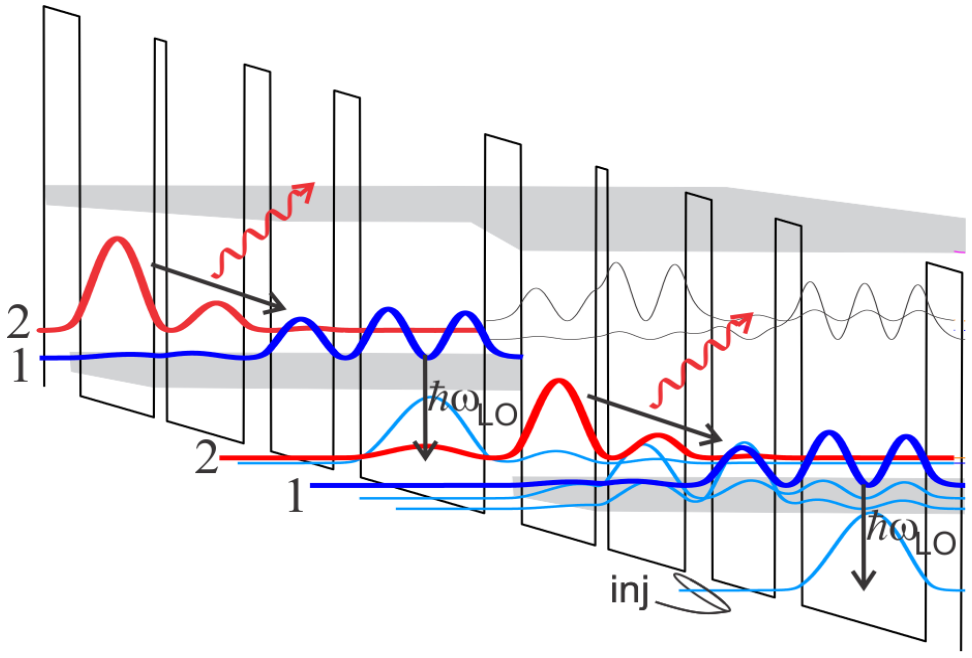

Figure 3-1: Electron transport through a biased four-well hybrid resonant-phonon active region. The squared magnitude of the wavefunctions for the sub-bands are shown. The upper lasing state 2 (red), the lower radiative state 1 (blue), and the injector states are indicated. The grey shaded areas correspond to minibands of states. This design uses LO-phonon scattering to depopulate the lower radiative state.

The following five active regions that will be discussed in the next session are based on the four-well hybrid resonant-phonon design of an $Al_{0.15}Ga_{0.85}As$/GaAs heterostructure, with a one-well injector state and a three-level continuum lower state. NGAS 1661-294 and VB0984 materials

contained 163 modules with a total thickness of about 10 μm and were designed to provide gain at 3.3 THz. Starting from the injection barrier, the layer thicknesses in Å for these two wafers are **51**/103/**17**/107/**37**/88/**37**/172 (barrier layers are bold). This design had provided working QCLs for several publications from this lab [85, 86] in the past. This new batches of wafers, however, produced different results than what was seen for the previous wafer (see the next section). VB0988 wafer, in contrast, consisted of 162 modules and was designed for 2.7 THz. VB1005 and VB1008 also contained 162 modules but were designed to lase at 2.3 THz. To provide gain at some specific frequency v, several key parameters, including energy levels, wavefunctions, and scattering rates must be properly engineered for the active region. Discussing the details of active region design is not the purpose of this work, but we should be aware that any inaccuracy in material design and/or material growth can lead to the shift of the resonance frequency in the QC gain medium.

3.2 Fabrication procedure

Here, I will describe the general procedure for fabricating QC metasurfaces. This fabrication process is summarized in Figure 3-2. For fabricating MM waveguide lasers, we follow the standard processes [87], which is similar to metasurface fabrication procedure, only with some skipped steps. We first deposit Ta (15 nm)/Cu (300 nm) on top of the highly-doped GaAs receiving wafer and the QCL wafer, and then we perform Cu-Cu thermocompression bonding using a mechanical clamp to bond these two chips. For this purpose, we use a laboratory oven (Carbolite Oven) at 350°C for 2 hours. We then deposit a ~300 nm SiO_2 layer on the back side of GaAs receiving

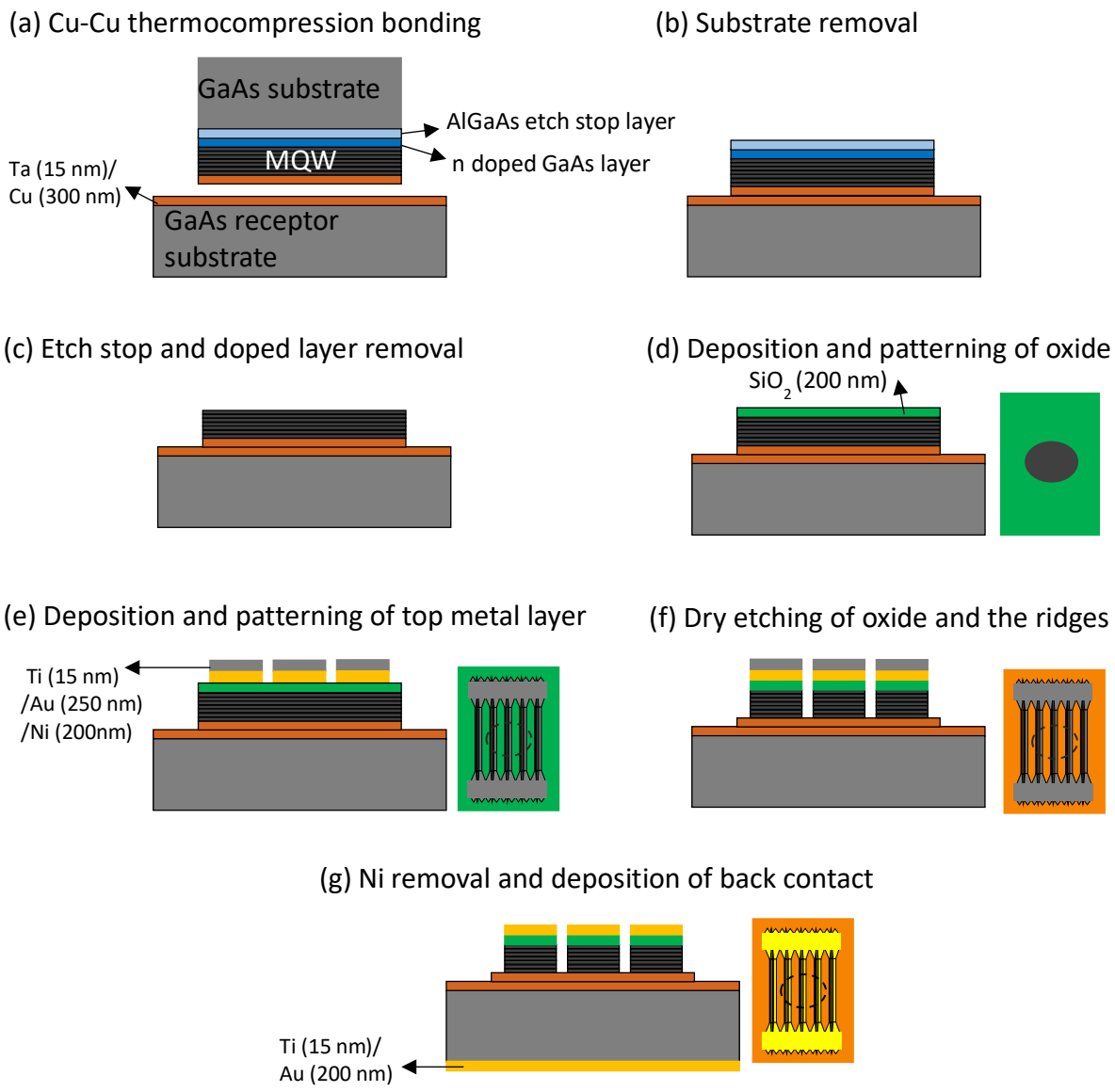

Figure 3-2: QC-metasurface fabrication procedure including the insulation layer deposition for selective biasing.

wafer to protect it against the following mechanical lapping and chemical etch (NH_4OH:H_2O_2 at a ratio of 1:25) steps to remove the substrate. In the next steps, we etch away the etch stop layer with a brief HF dip and remove the highly doped top contact to prevent current spreading into insulated

areas by chemical etching (H_2O_2:NH_4OH:H_2O at a ratio of 3:5:490). Then, a ~200 nm SiO_2 layer is deposited on the top as an insulation layer and then patterned to separate the bias area. The following step is evaporation, patterning, and lift-off of Ti/Au/Ni (15/250/200 nm) to provide the top metallization and the self-aligned etch mask. The metal-metal waveguide ridges are then defined by the Chlorine-based dry etch and removal of remaining Ni mask using a wet etchant. The last step is to deposit the Ti/Au (15/200 nm) back contact.

3.3 Characterization of QC Devices

3.3.1 Experimental setup

To measure the characteristics of a metal-metal waveguide laser or a QC-VECSEL, the fabricated devices are cleaved into small pieces. Each MM waveguide is typically 1 mm × 50-100 μm, and metasurfaces are 2-6 mm × 2-6 mm. We should cleave the MM waveguides very close to the laser's etched facets. Then, cleaved pieces are soldered onto a Cu chip carrier using indium and wire-bonded to electrically isolated, gold-coated Al_2O_3 pads on the chip carrier. The chip carrier is then attached to a cryostat mount. In the case of MM waveguide lasers, the mount is ideally attached to a Winston cone to collect the divergent beam. However, the Winston cone was mostly in use by my colleagues at the time of my experiments and therefore the following measurements were performed without the cone. The mount and the device are then placed in an Infrared (IR) Labs dewar with a HR silicon window. The output power is detected using a pyroelectric detector (Gentec) and calibrated using a thermopile, and the emission spectrum is measured using a Nicolet Fourier transform infrared spectrometer (FTIR) (see Figure 3-3).

To perform current, voltage, and power (*P-I-V*) measurements, the pyroelectric detector is mounted close to the cryostat, without any intermediate optics. To avoid device heating, we usually cool down the devices to 77 K and carry out *P-I-V* measurements in pulsed mode with 500ns pulses, repeated at 10 kHz (0.5% duty cycle). The pulsed currents and voltages are probed using a boxcar averager and the detector's signal is amplified using a lock-in amplifier. To measure spectrum of the laser, we replace the pyroelectric detector with an off-axis parabolic mirror to direct the divergent laser beam into the FTIR. As the mirror inside the FTIR is swept, the time dependent interference pattern is collected by the Ge:Ga detector (see Figure 3-3). This entire data acquisition is automated using LabView.

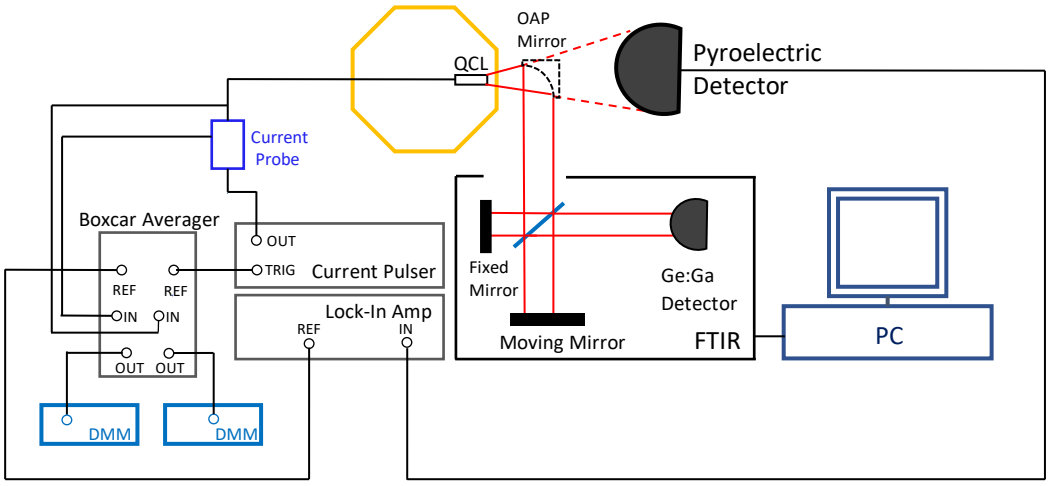

Figure 3-3: Experimental setup for measuring LIV and emission spectrum of a THz QC-ridge laser. We remove the OAP Mirror to measure power using a pyroelectric detector.

3.3.2 NGAS 1661-294 series of devices

P-I-V curves for a 100 μm × 1 mm MM waveguide laser and a uniform broadband metasurface with a bias diameter of 1 mm, which were fabricated using NGAS 1661-294 QC material, are shown in Figure 3-4 (a) and Figure 3-4 (c), respectively. The characteristics of the ridge laser were measured at 77 K and in pulsed mode with 1 µs-long pulses repeated at 15 kHz (1.5% duty cycle, modulated by a pulse train at 150 Hz) using lock-in detection. However, since the MM waveguide laser was not cleaved near its facet and it was not attached to a Winston cone, the output power was very low, and its peak value could not be accurately calibrated using the thermopile detector. *dI/dV* curve (versus current) is also plotted for this device in Figure 3-4 (c) to emphasize the three distinct slopes in the *I-V* curve. We also measured the laser's emission spectrum using the FTIR, and observed very clear peaks at 3.26 THz, 3.30 THz, 3.44 THz, and 3.55 THz.

The broadband metasurface was built into a VECSEL configuration with a high reflectivity (inductive) output coupler (R > 97%). To characterize the VECSEL, the output coupler was mounted inside the cryostat on a single axis piezoelectric stepping stage, and the piezoelectric stage was operated with an open-loop controller. The metasurface and the output coupler were aligned using a He:Ne laser. The *P-I-V* characteristics of the QC-VECSEL were then measured at 77 K and in pulsed mode with 500 ns-long pulses repeated at 10 kHz (0.5% duty cycle, modulated at 150 Hz). A clear *P-I* curve was detected by the pyro-electric detector, but a very low peak power (8 mW) was measured by the thermopile. This value is very small, considering that this device is dissipating a very large electrical power (~76 W). This large power dissipation prevented continuous-wave operation.

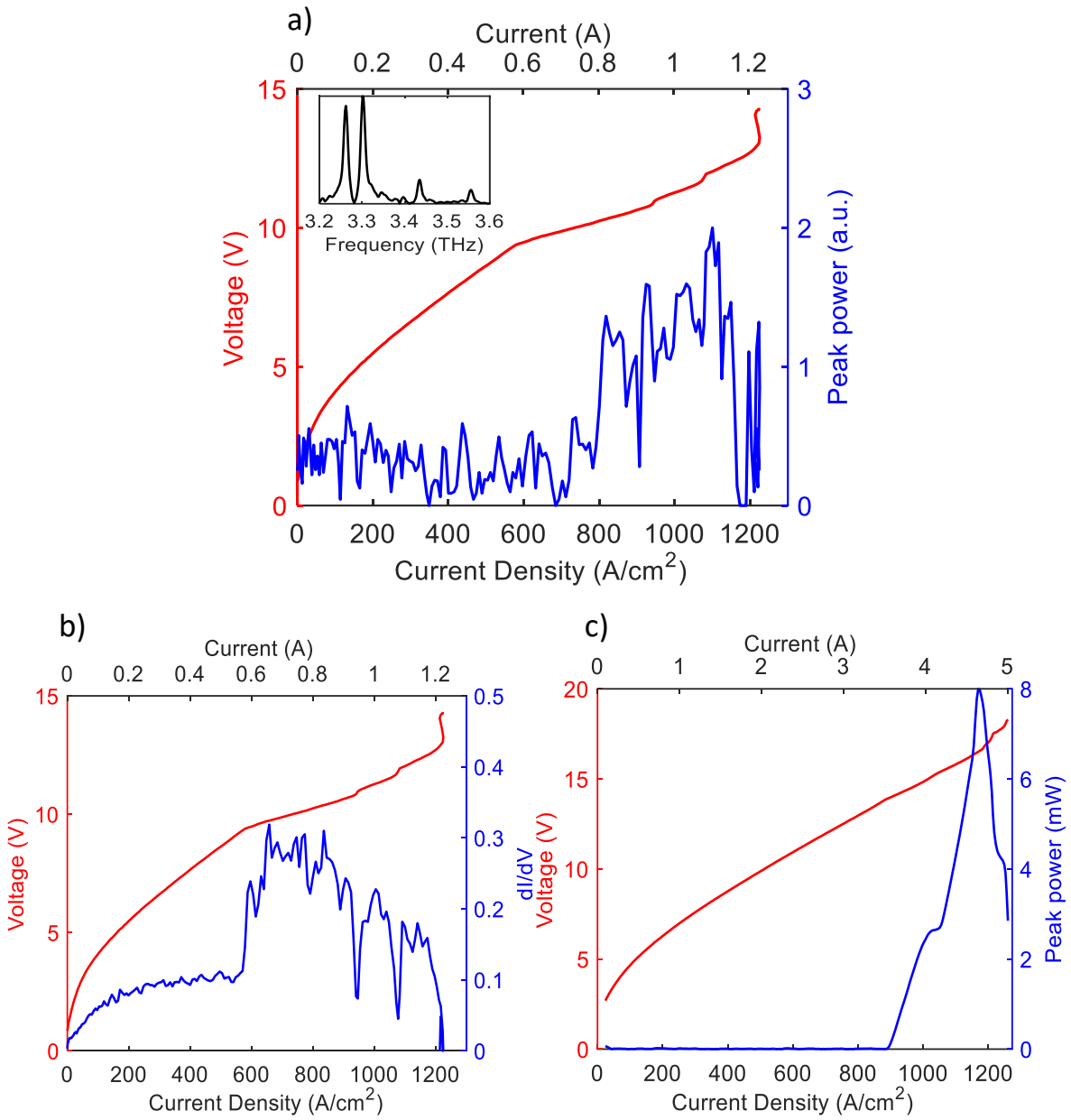

Figure 3-4: a) Pulsed-mode voltage and power vs. current characteristics at 77 K for a 100 μm × 1 mm MM ridge laser. Inset figure shows the emission spectrum of this laser. b) *dI/dV* versus current shows the three distinct regions in the I-V curve. c) Pulsed-mode voltage and power vs. current characteristics at 77 K for a QC-VECSEL which incorporates a broadband uniform metasurface with a 1.0 mm bias diameter and a highly reflective output coupler ($T < 3\%$). Both lasers use the NGAS 1661-294 active region.

Emission spectra of the QC-VECSEL was also measured as the piezoelectric stage was stepping away from the device, and therefore, the cavity was continuously getting larger (the change is quite small though compared to the cavity length). The spectra were collected over a single cavity length. A ~80 GHz continuous tuning of the laser frequency was observed near 3.8 THz, which was limited by the FSR of the external cavity (see Figure 3-5). We, therefore, estimated that the length of the external cavity was ~1.9 mm and the total change in cavity length was ~ 4×40 μm = 160 μm (when cavity length changes by half a wavelength, the frequency of the mode changes by one FSR) . As you can see in Figure 3-5, we do not observe any modes near 3.6 THz. Since this cavity was entirely mounted inside the cryostat, the atmospheric absorption loss had no effect on the cavity. Also, based on the previous simulations performed by my colleagues, the absorption loss in a 100 μm thick, highly-reflective output coupler does not vary much across the 3-4 THz range of frequencies, and the transmission also does not vary significantly across 3.4-3.6 THz. Observing no modes near 3.6 THz cannot be related to these two factors, and therefore, we anticipate that there is no gain from the QCL active material at this frequency.

Based on the obtained results, we concluded that there were three problems and uncertainties with this active region. First, the detected optical power was very low for the broadband metasurface despite its large power consumption. We should note that we were using a highly-reflective output coupler for these measurements, which means that the power could be up to 20 times larger, compared to when a low reflectivity output coupler is used ($R \approx 80\%$). Therefore, the output optical power might not be as low as it seems. Considering its current draw, however, we could still expect a larger output power. Secondly, the *I-V* (also *dI/dV*) curve for the ridge laser showed three distinct regions after the lasing threshold. We anticipated that this strange

behavior was due to some high-field domain formation within the active region, possibly because of nonuniformity over the 10 μm growth. And lastly, the large current densities that were measured for this wafer meant that this wafer is not very suitable for large area devices and for CW operation.

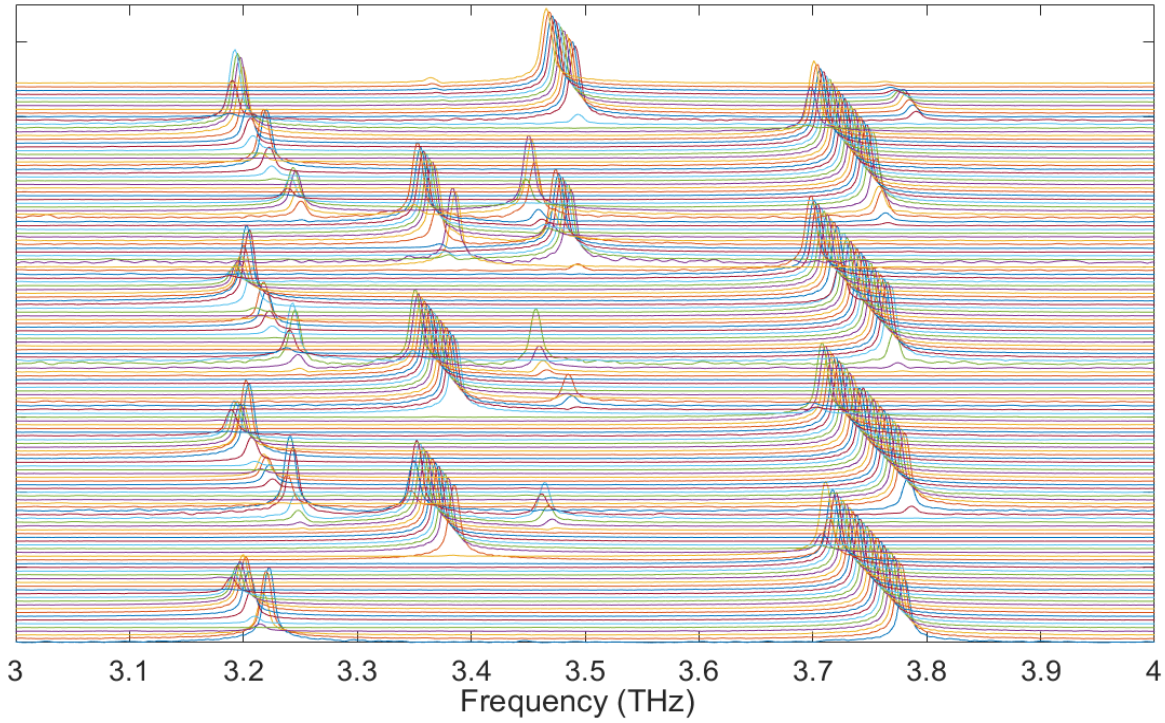

Figure 3-5: Normalized FTIR spectra collected as the VECSEL cavity length is tuned via a piezoelectric stepping stage**.**

3.3.3 VB0984 series of devices

Voltage and *dI/dV* curves versus current are shown in Figure 3-6 for a 50 μm × 1 mm MM ridge laser. The characteristics of the ridge laser were measured in pulsed mode with 500 ns-long pulses repeated at 10 kHz (0.5% duty cycle). Since the power consumption was very low, the output power was also so small that could not be detected by the pyroelectric detector. We did not have access to helium at the time of these measurements to use the sensitive helium cooled gallium-

doped germanium (Ge:Ga) photodetector. Therefore, we only measured the laser emission spectrum with the FTIR. FTIR's detector (Ge:Ga detector) is more sensitive than the pyro-electric detector, so we were able to collect the spectrum in CW mode. This wafer is very suitable for CW operations because of its very low power consumption, but it was not a good candidate for the purpose of this thesis since it lased at much higher frequencies (3.75-4.05 THz) than what we desired.

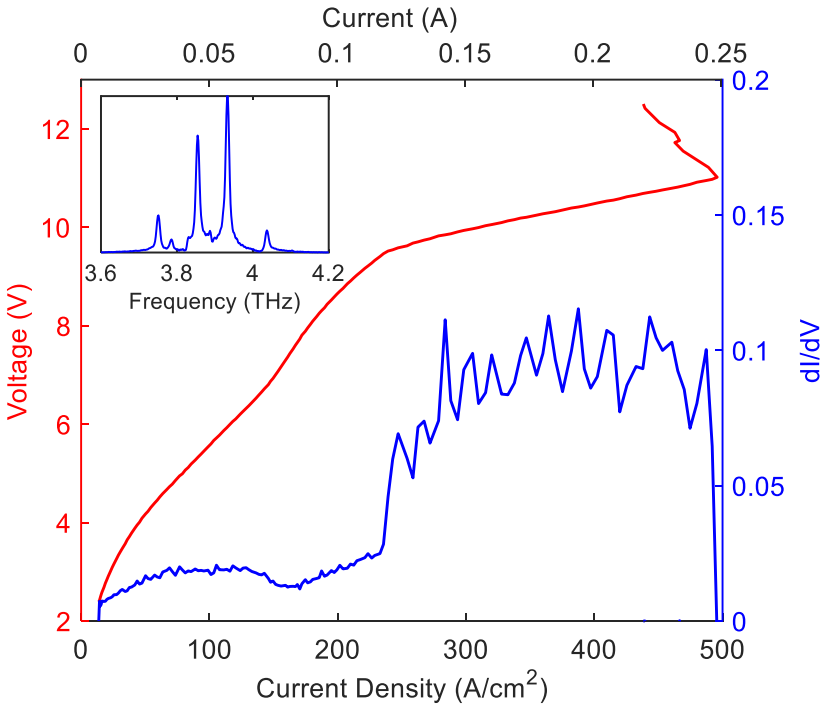

Figure 3-6: Pulsed-mode voltage and *dI/dV* vs. current characteristics at 77 K for a 50 μm × 1 mm MM waveguide laser. Inset of the figure shows the emission spectrum of this laser. This laser was fabricated using the VB0984 active region.

3.3.4 VB0988 series of devices

Using VB0988 active region, I fabricated a 50 μm × 1 mm MM ridge laser, and my colleague, Christopher Curwen, fabricated a similar 75 μm × 1 mm MM ridge. *I-V* characteristics of these two lasers are shown in Figure 3-7 and Figure 3-8, respectively. The characteristics of the 50 μm × 1 mm MM ridge were measured in pulsed mode with 500 ns-long pulses repeated at 10 kHz

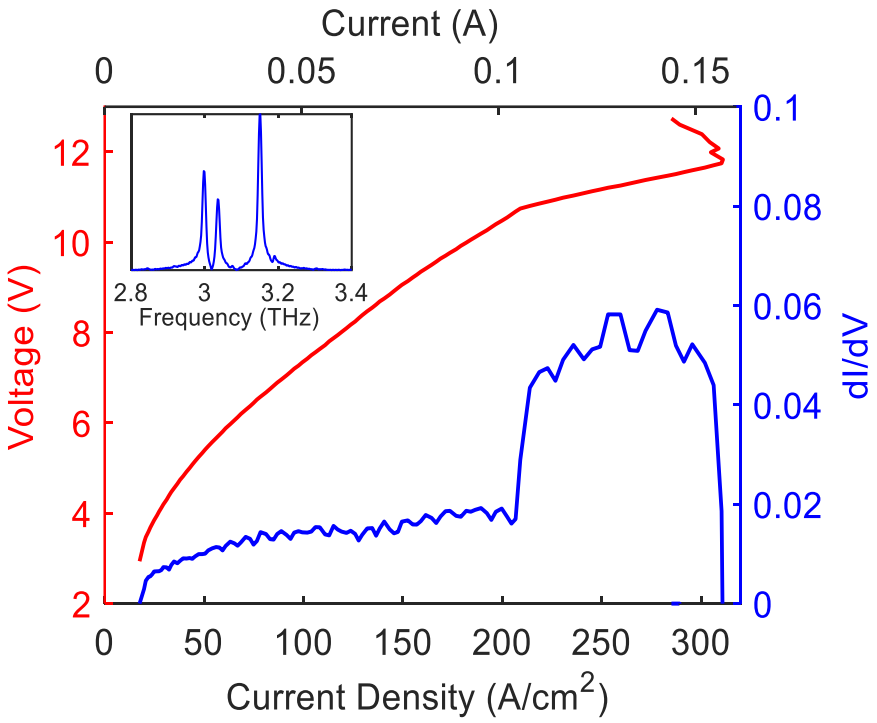

Figure 3-7: Pulsed-mode voltage and *dI/dV* vs. current characteristics at 77 K for a 50 μm × 1 mm MM waveguide laser which was fabricated by the author of this work, using the VB0988 active material. Inset of the figure shows the emission spectrum of this laser.

(0.5% duty cycle), and the 75 μm × 1 mm MM ridge characteristics were measured with 5% duty cycle. As you can see in the figures, the current densities that I have measured are much lower than what my colleague has measured. We anticipated that the 50 μm × 1 mm laser was only

partially biased due to an imperfect adhesion of the top metal contact. Again, I was not able to collect any power using the pyroelectric detector even in CW mode, so I only measured the laser emission spectrum with the FTIR.

My colleague, however, could collect a very low output power (~ 0.07 mW) in pulsed mode (5% duty cycle). Even though the measured output power was very small, the emission spectrum of this laser was very broad and was in our desired range of frequencies (~3 THz-3.4 THz). Therefore, we concluded that this wafer was the most suitable material among the available wafers for developing broadband Littrow metasurface ECLs. Large area metasurfaces and blazed grating metasurfaces, as those described in chapter 2, were fabricated using this material. However, those devices did not work due to multiple fabrication-related complications. Nonetheless, this material remains a good candidate for future grating metasurfaces.

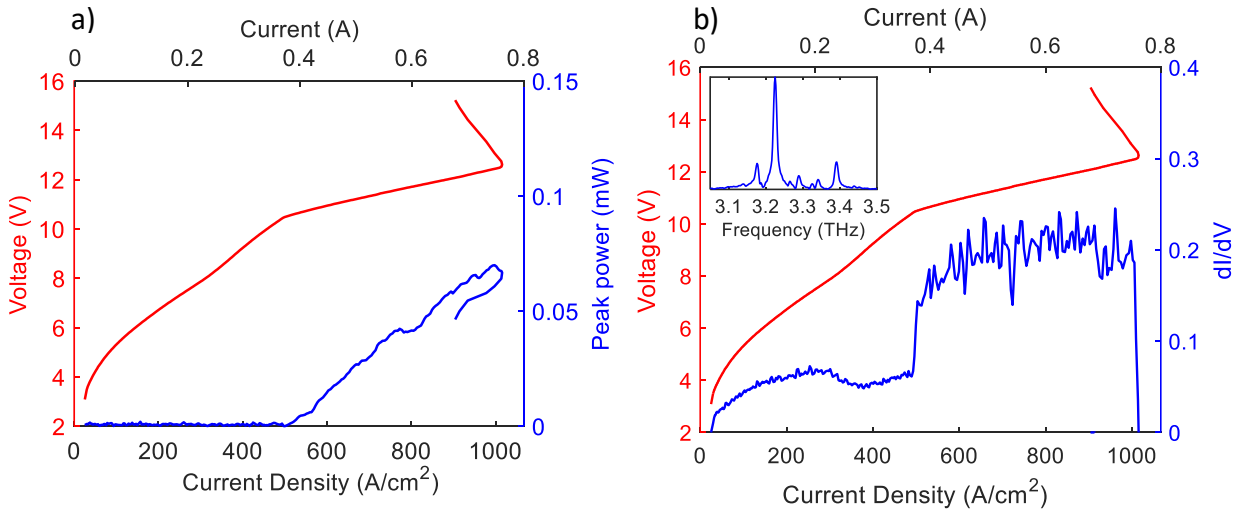

Figure 3-8: a) Power-current-voltage characteristics of a 75 μm × 1 mm MM waveguide laser, measured at 77 K. b) *dI/dV* vs. current and the emission spectrum of the laser. This laser was fabricated using VB0988 wafer by Christopher Curwen.

3.3.5 VB1005 series of devices

Voltage versus current density (*J*-*V*) curve for a 50 μm × 1 mm MM ridge laser (laser 1) and a 100 μm × 1 mm ridge laser (laser 2) are shown in Figure 3-9. These two lasers were fabricated in two different rounds. The characteristics of both lasers were measured in pulsed mode with 500 ns-long pulses repeated at 10 kHz (0.5% duty cycle). Since the power consumptions were very

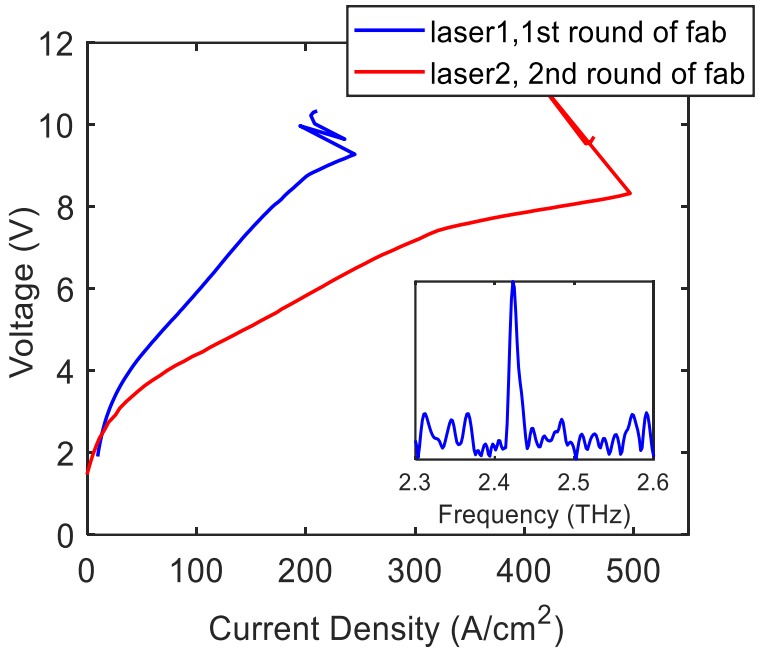

Figure 3-9: Pulsed-mode voltage vs. current density characteristics at 77 K for a 50 μm × 1 mm MM waveguide laser (laser 1) and a 100 μm × 1 mm laser (laser 2), which were fabricated using the VB1005 active material. Inset of the figure shows the emission spectrum of laser 1.

low, the output powers could not be detected by the pyroelectric detector. Therefore, we only measured the emission spectrum of laser 1 with the FTIR. Our FTIR was not working later when characteristics of laser 2 were being measured, so we could not measure its emission spectrum. As you see in the figure, laser 1 operated in much lower range of current densities. We, therefore,

assumed that laser 1 was only partially biased due to a faulty fabrication. Measured characteristics for Laser 2, however, were more reliable since one of my other labmates got similar results later for this active region. This active region is suitable for CW operations because of its very low power consumption, but it was not a good candidate for the purpose of this thesis since it lased at a much lower frequency (2.4 THz) than what we needed.

3.3.6 VB1008 series of devices

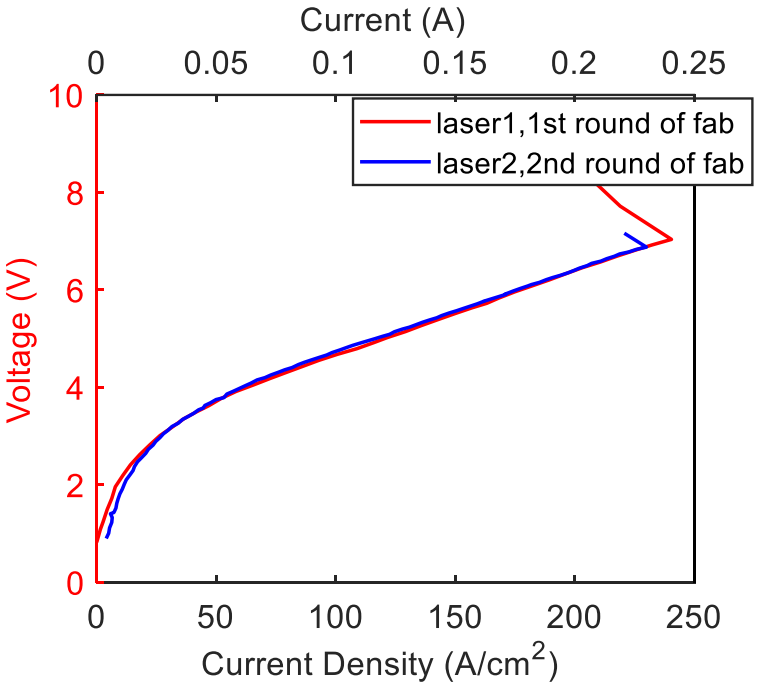

Figure 3-10: Pulsed-mode voltage vs. current characteristics of two 100 μm × 1 mm MM waveguide lasers measured in pulsed mode and at 77 K. These lasers were fabricated using the VB1008 active material.

I-V characteristics for two 100 μm × 1 mm ridge lasers are shown in Figure 3-10. These lasers were made in two separate rounds of fabrication. However, they showed similar

characteristics and none of them lased. These measurements were performed in pulsed mode with 500 ns-long pulses repeated at 10 kHz (0.5% duty cycle). We concluded that this active region does not lase because of growth-related problems.

Chapter 4: Conclusions and future work

4.1 Summary of metasurface design

The purpose of this study was to design and investigate tunable THz Littrow external-cavity quantum-cascade lasers based upon active metasurfaces. To realize tunable metasurface-based QCLs, two potential schemes were considered: a Littrow metasurface ECL and a 2nd-order blazed Littrow metasurface ECL. In the first model, the optical components are placed outside of the cryostat so that the laser cavity could be much longer than conventional QCLs. Conducted electromagnetic simulations and numerical models based on Fox-and-Li method confirmed the feasibility of this approach, albeit with somewhat increased values for the threshold gain. However, this approach requires large area metasurfaces (6.3 mm × 6.3 mm and 3.8 mm × 4 mm) with large circular bias areas (3.2 mm in diameter and 2.0 mm in diameter, respectively). The large power consumption of these devices would prevent CW operation, and would limit the tunability of the proposed Littrow metasurface ECL to pulsed mode condition. Also, the large spectral resolution of the grating (compared to FSR) could potentially result in a multi-mode laser, which in return limits the applications of this laser to solid-state absorption spectroscopy and imaging.

To develop tunable QCLs, a novel technique based on blazed metasurface gratings was also proposed and studied. For this approach, a periodic 4.3 mm × 4.3 mm metasurface with an elliptical bias area (a = 1 mm , b = 1.4 mm), containing three resonators in its unit cell, was designed for blazing on the 2nd diffraction order. The 2nd-order blazed Littrow metasurface ECL

was investigated using electromagnetic simulations and Fox-and-Li models. Ray tracing simulations were also performed to ensure the laser cavity stability. To make the implementation of this laser easier and the optical alignments less challenging, the entire cavity was designed to be constructed within a cryostat. Compared to the previous approach, the 2nd-order blazed Littrow metasurface ECL benefits from a fixed output laser beam, which makes the detection scheme simpler and easier. The main drawback of this technique, however, is the possibility of multi-moding, like the previous scheme. Also, the large power consumption for the proposed metasurface grating would limit its operation to pulsed mode, unless we use a QC active material which draws lower currents compared to the typical values. However, it is much easier to obtain lasing in this case, compared to the 1st-order Littrow metasurface ECL, due to great reduction in losses.

4.2 Summary of QC material characterization

In addition to designing the required metasurfaces and the laser cavities, we also needed to select a broadband QC gain material with desirable characteristics (low power consumptions, high output powers) to construct our tunable Littrow ECLs. Several MM waveguide lasers and a QC-VECSEL were fabricated, as test devices, using five candidate QC materials. The previously discussed large area QC metasurfaces and metasurface gratings were in fact designed based on the collected data from these devices. Among the five materials, NGAS 1661-294 and VB0988 wafers lased in our desired range of frequencies, but each had some problems. The optical powers that were collected for these devices were small compared to their large power dissipation. Also, the current-voltage characteristics of NGAS 1661-294 showed three distinct regions (slopes) after the lasing threshold, which was an unexpected behavior.

Therefore, we initially thought that VB0988 was the most promising material. Several attempts were made to fabricate large area metasurfaces and blazed metasurface gratings using this wafer. But none of the devices worked. Their current-voltage characteristics showed uncharacteristically large impedances, and devices would burn out during operation unexpectedly. However, we anticipated that this behavior was due to fabrication-related problems since I had encountered with several complications during the fabrication process. First, the yield after thermo-compression bonding using the mechanical clamp was very low. I had to use larger dies because I was fabricating larger metasurfaces than usual. But after substrate removal, only a small portion of the wafer would survive. Metal adhesion was the second issue. After placing the pieces in the dry etcher, the deposited Ti/Au/Ni layer on some of the ridges would peel off. And lastly, the Chlorine-based dry etch was not ideal. Many unetched micropillars were scattered across the surface of the die after the etch. These last two problems were most probably caused because of not properly cleaned surfaces. Although the devices that survived the fabrication looked normal, we anticipated that an insulating layer might be between the QC material and the top contact which prevents the device from being biased properly. In addition to fabrication problems, we had also noticed discolored areas on the original 4" VB0988 wafer. This could be a sign of a non-uniform growth and could explain the discrepancy between my results and results that my colleague had obtained. Nonetheless, the failures in fabricating a good lasing device should be considered unrelated to the potential success of the designs that were presented in this work. We're currently in the process of fabricating new devices using NGAS 1661-294 material, and at the same time obtaining new growths that could demonstrate better *P-I-V* characteristics.

4.3 Prospects for future QC Littrow metasurface external cavity lasers

While we should try to fabricate the metasurfaces that were discussed in this thesis again and try to construct Littrow metasurface external cavity lasers, further work must be done to realize high-performance lasers. The projected performance of the two designs that were discussed previously is mainly limited due to the large spectral resolution of the bulk diffracting grating or the metasurface grating. To develop single-mode tunable lasers, we should look into novel designs of metasurfaces that could generate larger beams on the gratings (using a larger bias area) without scaling the power consumption. We could, for example, use patch array metasurfaces to reduce the power consumption and thermal density (as shown in Figure 4-1 (c)). Also, we must use QC gain materials in our lasers that demonstrate preferable *P-I-V* characteristics. We can also obtain or fabricate a customized bulk diffraction grating that has a smaller period and blazes exactly at our desired range of frequencies to maximize the efficiency.

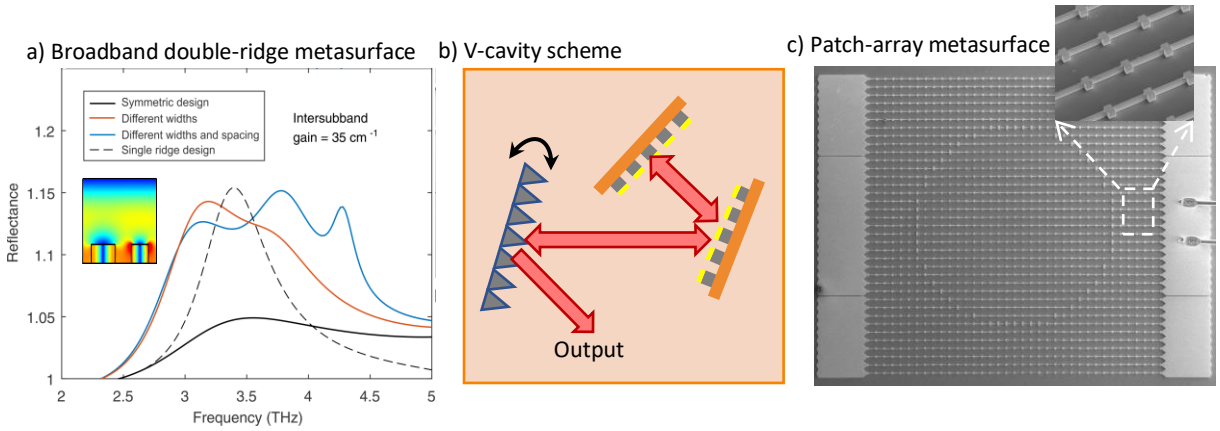

Figure 4-1: (a) Reflectance of a broadband coupled-resonator metasurface, designed by Christopher Curwen. b) A potential v-cavity scheme that could be implemented to increase the output power. c) A patch-array metasurface fabricated by Christopher Curwen.

To realize wider tunability and larger output powers in Littrow metasurface ECLs, we can investigate more complex cavity designs (e.g. v-cavity) that utilize multi metasurfaces, which could achieve an octave spanning gain and generate a large output power in combination. Also, using the same coupled-resonator approach that was presented in chapter 2, we could engineer alternative metasurfaces to achieve broader gain bandwidths. Examples of these two approaches are depicted in Figure 4-1. Additionally, further work must be done to reduce the losses, especially in external cavity lasers that will be constructed outside of the cryostat. We can, for example, develop low-loss AR-coated cryostat windows by dry-etching micropillars on a silicon substrate to form an effective λ/4 layer with an effective index $\sqrt{n}$. Also, we can reduce the atmospheric losses by minimizing the humidity using nitrogen gas purging.

References

[1] B. S. Williams, "Terahertz quantum-cascade lasers," *Nature Photonics,* vol. 1, no. 9, pp. 517-525, 2007/09/01 2007.

[2] I. Mehdi, G. Chattopadhyay, E. Schlecht, J. Ward, J. Gill, F. Maiwald, and A. Maestrini, "Terahertz multiplier circuits," in *2006 IEEE MTT-S International Microwave Symposium Digest*, 2006: IEEE, pp. 341-344.

[3] P. H. Siegel, "Terahertz technology," *IEEE Transactions on Microwave Theory and Techniques,* vol. 50, no. 3, pp. 910-928, 2002.

[4] R. Köhler, A. Tredicucci, F. Beltram, H. E. Beere, E. H. Linfield, A. G. Davies, D. A. Ritchie, R. C. Iotti, and F. Rossi, "Terahertz semiconductor-heterostructure laser," *Nature,* vol. 417, no. 6885, pp. 156-159, 2002.

[5] S. Kumar, "Recent Progress in Terahertz Quantum Cascade Lasers," *IEEE Journal of Selected Topics in Quantum Electronics,* vol. 17, no. 1, pp. 38-47, 2011.

[6] L. Li, L. Chen, J. Zhu, J. Freeman, P. Dean, A. Valavanis, A. Davies, and E. Linfield, "Terahertz quantum cascade lasers with> 1 W output powers," *Electronics letters,* vol. 50, no. 4, pp. 309-311, 2014.

[7] L. Li, I. Kundu, P. Dean, E. H. Linfield, and A. G. Davies, "High-power GaAs/AlGaAs quantum cascade lasers with emission in the frequency range 4.7–5.6 THz," 2016: Leeds.

[8] Y.-Y. Li, J.-Q. Liu, F.-Q. Liu, J.-C. Zhang, S.-Q. Zhai, N. Zhuo, L.-J. Wang, S.-M. Liu, and Z.-G. Wang, "High power-efficiency terahertz quantum cascade laser," *Chinese Physics B,* vol. 25, no. 8, p. 084206, 2016.

[9] M. S. Vitiello, G. Scalari, B. Williams, and P. De Natale, "Quantum cascade lasers: 20 years of challenges," *Optics express,* vol. 23, no. 4, pp. 5167-5182, 2015.

[10] L. Bosco, M. Franckié, G. Scalari, M. Beck, A. Wacker, and J. Faist, "Thermoelectrically cooled THz quantum cascade laser operating up to 210 K," *Applied Physics Letters,* vol. 115, no. 1, p. 010601, 2019.

[11] L. H. Li, L. Chen, J. R. Freeman, M. Salih, P. Dean, A. G. Davies, and E. H. Linfield, "Multi-Watt high-power THz frequency quantum cascade lasers," *Electronics Letters,* vol. 53, no. 12, pp. 799-800, 2017.

[12] B. S. Williams, S. Kumar, Q. Hu, and J. L. Reno, "High-power terahertz quantum-cascade lasers," *Electronics Letters,* vol. 42, no. 2, pp. 89-91, 2006.

[13] B. S. Williams, S. Kumar, H. Callebaut, Q. Hu, and J. L. Reno, "Terahertz quantum-cascade laser at $\lambda \approx 100$ μ m using metal waveguide for mode confinement," *Applied Physics Letters,* vol. 83, no. 11, pp. 2124-2126, 2003.

[14] S. Kohen, B. S. Williams, and Q. Hu, "Electromagnetic modeling of terahertz quantum cascade laser waveguides and resonators," *Journal of applied physics,* vol. 97, no. 5, p. 053106, 2005.

[15] A. W. M. Lee, Q. Qin, S. Kumar, B. S. Williams, Q. Hu, and J. L. Reno, "High-power and high-temperature THz quantum-cascade lasers based on lens-coupled metal-metal waveguides," *Optics letters,* vol. 32, no. 19, pp. 2840-2842, 2007.

[16] T.-Y. Kao, Q. Hu, and J. L. Reno, "Phase-locked arrays of surface-emitting terahertz quantum-cascade lasers," *Applied Physics Letters,* vol. 96, no. 10, p. 101106, 2010.

[17] M. Amanti, M. Fischer, G. Scalari, M. Beck, and J. Faist, "Low-divergence single-mode terahertz quantum cascade laser," *Nature Photonics,* vol. 3, no. 10, p. 586, 2009.

[18] Y. Chassagneux, R. Colombelli, W. Maineult, S. Barbieri, H. Beere, D. Ritchie, S. Khanna, E. Linfield, and A. G. Davies, "Electrically pumped photonic-crystal terahertz lasers controlled by boundary conditions," *Nature,* vol. 457, no. 7226, pp. 174-178, 2009.

[19] L. Xu, C. A. Curwen, D. Chen, J. L. Reno, T. Itoh, and B. S. Williams, "Terahertz metasurface quantum-cascade VECSELs: Theory and performance," *IEEE Journal of Selected Topics in Quantum Electronics,* vol. 23, no. 6, pp. 1-12, 2017.

[20] S. Kumar, B. S. Williams, Q. Qin, A. M. Lee, Q. Hu, and J. L. Reno, "Surface-emitting distributed feedback terahertz quantum-cascade lasers in metal-metal waveguides," *Optics Express,* vol. 15, no. 1, pp. 113-128, 2007.

[21] S. P. Khanna, M. Salih, P. Dean, A. G. Davies, and E. H. Linfield, "Electrically tunable terahertz quantum-cascade laser with a heterogeneous active region," *Applied Physics Letters,* vol. 95, no. 18, p. 181101, 2009.

[22] C. Gmachl, D. L. Sivco, R. Colombelli, F. Capasso, and A. Y. Cho, "Ultra-broadband semiconductor laser," *Nature,* vol. 415, no. 6874, pp. 883-887, 2002.

[23] M. S. Vitiello and A. Tredicucci, "Tunable emission in THz quantum cascade lasers," *IEEE Transactions on Terahertz Science and Technology,* vol. 1, no. 1, pp. 76-84, 2011.

[24] Q. Qin, B. S. Williams, S. Kumar, J. L. Reno, and Q. Hu, "Tuning a terahertz wire laser," *Nature photonics,* vol. 3, no. 12, p. 732, 2009.

[25] Q. Qin, J. L. Reno, and Q. Hu, "MEMS-based tunable terahertz wire-laser over 330 GHz," *Optics letters,* vol. 36, no. 5, pp. 692-694, 2011.

[26] C. A. Curwen, J. L. Reno, and B. S. Williams, "Broadband continuous single-mode tuning of a short-cavity quantum-cascade VECSEL," *Nature Photonics,* vol. 13, no. 12, pp. 855-859, 2019.

[27] A. Hugi, R. Terazzi, Y. Bonetti, A. Wittmann, M. Fischer, M. Beck, J. Faist, and E. Gini, "External cavity quantum cascade laser tunable from 7.6 to 11.4 μ m," *Applied Physics Letters,* vol. 95, no. 6, p. 061103, 2009.

[28] N. Bonod and J. Neauport, "Diffraction gratings: from principles to applications in high-intensity lasers," *Adv. Opt. Photon.,* vol. 8, no. 1, pp. 156-199, 2016/03/31 2016.

[29] C. A. Palmer and E. G. Loewen, *Diffraction grating handbook*. Newport Corporation New York, 2005.

[30] B. Meng and Q. J. Wang, "Broadly tunable single-mode mid-infrared quantum cascade lasers," *Journal of Optics,* vol. 17, no. 2, p. 023001, 2015.

[31] G. Luo, C. Peng, H. Le, S. Pei, W.-Y. Hwang, B. Ishaug, J. Um, J. N. Baillargeon, and C.-H. Lin, "Grating-tuned external-cavity quantum-cascade semiconductor lasers," *Applied Physics Letters,* vol. 78, no. 19, pp. 2834-2836, 2001.

[32] R. Maulini, A. Mohan, M. Giovannini, J. Faist, and E. Gini, "External cavity quantum-cascade laser tunable from 8.2 to 10.4 μ m using a gain element with a heterogeneous cascade," *Applied physics letters,* vol. 88, no. 20, p. 201113, 2006.

[33] M. Pushkarsky, A. Tsekoun, I. G. Dunayevskiy, R. Go, and C. K. N. Patel, "Sub-parts-per-billion level detection of NO2 using room-temperature quantum cascade lasers," *Proceedings of the National Academy of Sciences,* vol. 103, no. 29, pp. 10846-10849, 2006.

[34] E. Mujagić, C. Schwarzer, Y. Yao, J. Chen, C. Gmachl, and G. Strasser, "Two-dimensional broadband distributed-feedback quantum cascade laser arrays," *Applied physics letters,* vol. 98, no. 14, p. 141101, 2011.

[35] T. S. Mansuripur, S. Menzel, R. Blanchard, L. Diehl, C. Pflügl, Y. Huang, J.-H. Ryou, R. D. Dupuis, M. Loncar, and F. Capasso, "Widely tunable mid-infrared quantum cascade lasers using sampled grating reflectors," *Optics express,* vol. 20, no. 21, pp. 23339-23348, 2012.

[36] P. Fuchs, J. Seufert, J. Koeth, J. Semmel, S. Höfling, L. Worschech, and A. Forchel, "Widely tunable quantum cascade lasers with coupled cavities for gas detection," *Applied Physics Letters,* vol. 97, no. 18, p. 181111, 2010.

[37] B. Meng, J. Tao, X. Hui Li, Y. Quan Zeng, S. Wu, and Q. Jie Wang, "Tunable single-mode slot waveguide quantum cascade lasers," *Applied Physics Letters,* vol. 104, no. 20, p. 201106, 2014.

[38] T. Tsai and G. Wysocki, "External-cavity quantum cascade lasers with fast wavelength scanning," *Applied Physics B,* vol. 100, no. 2, pp. 243-251, 2010.

[39] Y. V. Flores, M. Haertelt, S. Hugger, L. Butschek, C. Schilling, A. Merten, M. Schwarzenberg, A. Dreyhaupt, J. Grahmann, M. Rattunde, and R. Ostendorf, "Advances in MOEMS-based External Cavity QCLs," in *2019 Conference on Lasers and Electro-Optics Europe and European Quantum Electronics Conference*, Munich, 2019: Optical Society of America, p. cb_7_5.

[40] R. Ostendorf, L. Butschek, A. Merten, J. Grahmann, J. Jarvis, S. Hugger, F. Fuchs, and J. Wagner, "Real-time spectroscopic sensing using a widely tunable external cavity-QCL

with MOEMS diffraction grating," in *Quantum Sensing and Nano Electronics and Photonics XIII*, 2016, vol. 9755: International Society for Optics and Photonics, p. 975507.

[41] A. W. M. Lee, B. S. Williams, S. Kumar, Q. Hu, and J. L. Reno, "Tunable terahertz quantum cascade lasers with external gratings," *Optics Letters,* vol. 35, no. 7, pp. 910-912, 2010/04/01 2010.

[42] G. N. Rao and A. Karpf, "External cavity tunable quantum cascade lasers and their applications to trace gas monitoring," *Applied optics,* vol. 50, no. 4, pp. A100-A115, 2011.

[43] S. Bartalini, L. Consolino, P. Cancio, P. De Natale, P. Bartolini, A. Taschin, M. De Pas, H. Beere, D. Ritchie, and M. Vitiello, "Frequency-comb-assisted terahertz quantum cascade laser spectroscopy," *Physical Review X,* vol. 4, no. 2, p. 021006, 2014.

[44] A. Barkan, F. K. Tittel, D. M. Mittleman, R. Dengler, P. H. Siegel, G. Scalari, L. Ajili, J. Faist, H. E. Beere, and E. H. Linfield, "Linewidth and tuning characteristics of terahertz quantum cascade lasers," *Optics letters,* vol. 29, no. 6, pp. 575-577, 2004.

[45] R. Eichholz, H. Richter, S. Pavlov, M. Wienold, L. Schrottke, R. Hey, H. Grahn, and H.-W. Hübers, "Multi-channel terahertz grating spectrometer with quantum-cascade laser and microbolometer array," *Applied Physics Letters,* vol. 99, no. 14, p. 141112, 2011.

[46] H.-W. Hübers, S. Pavlov, H. Richter, A. Semenov, L. Mahler, A. Tredicucci, H. Beere, and D. Ritchie, "High-resolution gas phase spectroscopy with a distributed feedback terahertz quantum cascade laser," *Applied Physics Letters,* vol. 89, no. 6, p. 061115, 2006.

[47] M. S. Vitiello, L. Consolino, S. Bartalini, A. Taschin, A. Tredicucci, M. Inguscio, and P. De Natale, "Quantum-limited frequency fluctuations in a terahertz laser," *Nature Photonics,* vol. 6, no. 8, pp. 525-528, 2012/08/01 2012.

[48] H.-W. Hubers, M. F. Kimmitt, N. Hiromoto, and E. Brundermann, "Terahertz spectroscopy: System and sensitivity considerations," *IEEE Transactions on Terahertz Science and Technology,* vol. 1, no. 1, pp. 321-331, 2011.

[49] H.-W. Hübers, S. Pavlov, H. Richter, A. Semenov, L. Mahler, A. Tredicucci, H. Beere, and D. Ritchie, "Molecular spectroscopy with terahertz quantum cascade lasers," *Journal of Nanoelectronics and Optoelectronics,* vol. 2, no. 1, pp. 101-107, 2007.

[50] Y. Yang, D. Burghoff, D. J. Hayton, J.-R. Gao, J. L. Reno, and Q. Hu, "Terahertz multiheterodyne spectroscopy using laser frequency combs," *Optica,* vol. 3, no. 5, pp. 499-502, 2016.

[51] Y. Shen, a. T. Lo, P. Taday, B. Cole, W. Tribe, and M. Kemp, "Detection and identification of explosives using terahertz pulsed spectroscopic imaging," *Applied physics letters,* vol. 86, no. 24, p. 241116, 2005.

[52] H.-W. Hübers, S. Pavlov, A. Semenov, R. Köhler, L. Mahler, A. Tredicucci, H. Beere, D. Ritchie, and E. Linfield, "Terahertz quantum cascade laser as local oscillator in a heterodyne receiver," *Optics express,* vol. 13, no. 15, pp. 5890-5896, 2005.

[53] Y. Ren, J. Hovenier, R. Higgins, J. Gao, T. Klapwijk, S. Shi, B. Klein, T.-Y. Kao, Q. Hu, and J. Reno, "High-resolution heterodyne spectroscopy using a tunable quantum cascade laser around 3.5 THz," *Applied Physics Letters,* vol. 98, no. 23, p. 231109, 2011.

[54] J. Waldman, A. A. Danylov, T. M. Goyette, M. J. Coulombe, R. H. Giles, A. J. Gatesman, W. D. Goodhue, J. Li, K. J. Linden, and W. E. Nixon, "Prospects for quantum cascade lasers as transmitters and local oscillators in coherent terahertz transmitter/receiver

systems," in *Terahertz Technology and Applications II*, 2009, vol. 7215: International Society for Optics and Photonics, p. 72150C.

[55] D. J. Hayton, J. L. Kloosterman, J.-r. Gao, N. Vercruyssen, C. K. Walker, Q. Hu, and T.-Y. Kao, "A 4.7 THz HEB/QCL heterodyne receiver for STO-2," in *2014 39th International Conference on Infrared, Millimeter, and Terahertz waves (IRMMW-THz)*, 2014: IEEE, pp. 1-2.

[56] J. Silva, B. Mirzaei, W. Laauwen, N. More, A. Young, C. Kulesa, C. Walker, A. Khalatpour, Q. Hu, and C. Groppi, "4× 2 HEB receiver at 4.7 THz for GUSTO," in *Millimeter, Submillimeter, and Far-Infrared Detectors and Instrumentation for Astronomy IX*, 2018, vol. 10708: International Society for Optics and Photonics, p. 107080Z.

[57] S. Heyminck, U. Graf, R. Güsten, J. Stutzki, H. Hübers, and P. Hartogh, "GREAT: the SOFIA high-frequency heterodyne instrument," *Astronomy & Astrophysics*, vol. 542, p. L1, 2012.

[58] C. Risacher, R. Güsten, J. Stutzki, H. Hübers, D. Büchel, U. U. Graf, S. Heyminck, C. E. Honingh, K. Jacobs, B. Klein, T. Klein, C. Leinz, P. Pütz, N. Reyes, O. Ricken, H. Wunsch, P. Fusco, and S. Rosner, "First Supra-THz Heterodyne Array Receivers for Astronomy With the SOFIA Observatory," *IEEE Transactions on Terahertz Science and Technology*, vol. 6, no. 2, pp. 199-211, 2016.

[59] A. Baranov and E. Tournié, *Semiconductor Lasers: Fundamentals and Applications*. Elsevier, 2013.

[60] A. W. Lee, Q. Qin, S. Kumar, B. S. Williams, Q. Hu, and J. L. Reno, "Real-time terahertz imaging over a standoff distance (> 25 meters)," *Applied Physics Letters,* vol. 89, no. 14, p. 141125, 2006.

[61] P. Dean, M. U. Shaukat, S. P. Khanna, S. Chakraborty, M. Lachab, A. Burnett, G. Davies, and E. H. Linfield, "Absorption-sensitive diffuse reflection imaging of concealed powders using a terahertz quantum cascade laser," *Optics Express,* vol. 16, no. 9, pp. 5997-6007, 2008.

[62] P. Dean, N. K. Saat, S. P. Khanna, M. Salih, A. Burnett, J. Cunningham, E. H. Linfield, and A. G. Davies, "Dual-frequency imaging using an electrically tunable terahertz quantum cascade laser," *Optics express,* vol. 17, no. 23, pp. 20631-20641, 2009.

[63] L. A. Sterczewski, J. Westberg, Y. Yang, D. Burghoff, J. Reno, Q. Hu, and G. Wysocki, "Terahertz hyperspectral imaging with dual chip-scale combs," *Optica,* vol. 6, no. 6, pp. 766-771, 2019.

[64] A. W. Lee, B. S. Williams, S. Kumar, Q. Hu, and J. L. Reno, "Real-time imaging using a 4.3-THz quantum cascade laser and a 320/spl times/240 microbolometer focal-plane array," *IEEE Photonics Technology Letters,* vol. 18, no. 13, pp. 1415-1417, 2006.

[65] L. Xu, C. A. Curwen, P. W. Hon, Q.-S. Chen, T. Itoh, and B. S. Williams, "Metasurface external cavity laser," *Applied Physics Letters,* vol. 107, no. 22, p. 221105, 2015.

[66] M. Kuznetsov, F. Hakimi, R. Sprague, and A. Mooradian, "High-power (> 0.5-W CW) diode-pumped vertical-external-cavity surface-emitting semiconductor lasers with circular TEM/sub 00/beams," *IEEE Photonics Technology Letters,* vol. 9, no. 8, pp. 1063-1065, 1997.

[67] B. Rudin, A. Rutz, M. Hoffmann, D. Maas, A.-R. Bellancourt, E. Gini, T. Südmeyer, and U. Keller, "Highly efficient optically pumped vertical-emitting semiconductor laser with more than 20 W average output power in a fundamental transverse mode," *Optics letters,* vol. 33, no. 22, pp. 2719-2721, 2008.

[68] A. Tropper, H. Foreman, A. Garnache, K. Wilcox, and S. Hoogland, "Vertical-external-cavity semiconductor lasers," *Journal of Physics D: Applied Physics,* vol. 37, no. 9, p. R75, 2004.

[69] L. Xu, "Terahertz Metasurface Quantum Cascade Laser," *PhD Thesis, University of California, Los Angeles,* 2017.

[70] M. Memarian, X. Li, Y. Morimoto, and T. Itoh, "Wide-band/angle blazed surfaces using multiple coupled blazing resonances," *Scientific reports,* vol. 7, no. 1, pp. 1-12, 2017.

[71] A. G. Fox and T. Li, "Resonant modes in a maser interferometer," *Bell System Technical Journal,* vol. 40, no. 2, pp. 453-488, 1961.

[72] C. A. Curwen, "Development of Terahertz Quantum-Cascade VECSELs," *PhD Thesis, University of California Los Angeles, ,* 2019.

[73] M. Naftaly and R. Dudley, "Terahertz reflectivities of metal-coated mirrors," *Applied Optics,* vol. 50, no. 19, pp. 3201-3204, 2011/07/01 2011.

[74] S. Biber, D. Schneiderbanger, L.-P. Schmidt, M. Walther, B. Fischer, M. Schwarzer, and P. Jepsen, "Low loss silicon window material for submillimeter waves using micromachined artificial dielectrics for anti-reflection coating," in *Infrared and Millimeter Waves, Conference Digest of the 2004 Joint 29th International Conference on 2004 and 12th International Conference on Terahertz Electronics, 2004.*, 2004: IEEE, pp. 105-106.

[75] A. Rakić, T. Taimre, K. Bertling, Y. Lim, P. Dean, A. Valavanis, and D. Indjin, "Sensing and imaging using laser feedback interferometry with quantum cascade lasers," *Applied Physics Reviews*, vol. 6, no. 2, p. 021320, 2019.

[76] N. Yu and F. Capasso, "Flat optics with designer metasurfaces," *Nature Materials*, vol. 13, no. 2, pp. 139-150, 2014/02/01 2014.

[77] X. Li, M. Memarian, K. Dhwaj, and T. Itoh, "Blazed metasurface grating: The planar equivalent of a sawtooth grating," in *2016 IEEE MTT-S International Microwave Symposium (IMS)*, 2016: IEEE, pp. 1-3.

[78] M. Memarian, X. Li, and T. Itoh, "Resonant blazed metasurface gratings," in *2016 46th European Microwave Conference (EuMC)*, 2016: IEEE, pp. 297-300.

[79] E. Jull, J. Heath, and G. Ebbeson, "Gratings that diffract all incident energy," *JOSA*, vol. 67, no. 4, pp. 557-559, 1977.

[80] K. Jose and K. Nair, "Reflector-backed perfectly blazed strip gratings simulate corrugated reflector effects," *Electronics Letters*, vol. 23, no. 2, pp. 86-87, 1987.

[81] E. Popov, D. Maystre, and G. Tayeb, "Whispering gallery modes and other cavity modes for perfect backscattering and blazing," *JOSA A*, vol. 27, no. 7, pp. 1584-1592, 2010.

[82] (https://www.attocube.com/en/products/nanopositioners/low-temperature-nanopositioners/anr240reslt-rotator-360-endless).

[83] (https://www.thorlabs.com/thorproduct.cfm?partnumber=CM127-025-M01).

[84] (https://www.thorlabs.com/thorproduct.cfm?partnumber=MK05#ad-image-0).

[85] L. Xu, D. Chen, C. A. Curwen, M. Memarian, J. L. Reno, T. Itoh, and B. S. Williams, "Metasurface quantum-cascade laser with electrically switchable polarization," *Optica*, vol. 4, no. 4, pp. 468-475, 2017.

[86] L. Xu, C. A. Curwen, J. L. Reno, and B. S. Williams, "High performance terahertz metasurface quantum-cascade VECSEL with an intra-cryostat cavity," *Applied Physics Letters*, vol. 111, no. 10, p. 101101, 2017.

[87] B. S. Williams, S. Kumar, Q. Hu, and J. L. Reno, "Operation of terahertz quantum-cascade lasers at 164 K in pulsed mode and at 117 K in continuous-wave mode," *Optics Express*, vol. 13, no. 9, pp. 3331-3339, 2005/05/02 2005.